Guiding self-organized pattern formation in cell polarity establishment

Peter Gross[1,2,3,†], K. Vijay Kumar[4,3†], Nathan W. Goehring[5,6], Justin S. Bois[7], Carsten Hoege[2], Frank Jülicher[3], Stephan W. Grill[1,2,3*]

Affiliations: [1]BIOTEC, TU Dresden, Tatzberg 47/49, 01307, Dresden, Germany

[2]Max Planck Institute of Molecular Cell Biology and Genetics, Pfotenhauerstrasse 108, 01307 Dresden, Germany

[3]Max Planck Institute for the Physics of Complex Systems, Nöthnitzer Strasse 38, 01187 Dresden, Germany

[4]International Centre for Theoretical Sciences, Tata Institute of Fundamental Research, Bengaluru 560089, India

[5]The Francis Crick Institute, 1 Midland Road, London NW1 1AT, UK

[6]Medical Research Council Laboratory for Molecular Cell Biology, Gower Street, University College London, London WC1E 6BT, UK

[7]California Institute of Technology, 1200 E California Blvd, Pasadena, CA 91125, USA

[†]These authors contributed equally [*]To whom correspondence should be addressed; E-mail: stephan.grill@biotec.tu-dresden.de.

Abstract

Spontaneous pattern formation in Turing systems relies on feedback. But patterns in cells and tissues seldom form spontaneously — instead they are controlled by regulatory biochemical interactions that provide molecular guiding cues. The relationship between these guiding cues and feedback in controlled biological pattern formation remains unclear. Here, we explore this relationship during cell-polarity establishment in the one-cell-stage *C. elegans* embryo. We quantify the strength of two feedback systems that operate during polarity establishment: feedback between polarity proteins and the actomyosin cortex, and mutual antagonism among polarity proteins. We characterize how these feedback systems are modulated by guiding cues from the centrosome, an organelle regulating cell division. By coupling a mass-conserved Turing-like reaction–diffusion system for polarity proteins to an active-gel description of the actomyosin cortex, we reveal a transition point beyond which feedback ensures self-organized polarization, even when cues are removed. Notably, the system moves from a guide-dominated to a feedback-dominated regime well beyond this transition point, which ensures robustness. Together, these results reveal a general criterion for controlling biological pattern-forming systems: feedback remains subcritical to avoid unstable behaviour, and molecular guiding cues drive the system beyond a transition point for pattern formation.

Cell polarity establishment in *C. elegans* zygotes is a prototypical example for cellular pattern formation that depends both on feedback between two classes of pattern-forming proteins and on upstream guiding cues provided by the centrosomal polarity trigger [1–3]. Posterior PAR proteins (pPARs: PAR-1, PAR-2, and LGL-1) and anterior PAR proteins (aPARs: PAR-6, PAR-3, and PKC-3) interact via antagonistic feedback while bound to the cell cortex [4], which gives rise to stably unpolarized and polarized states [5–7]. The formation of PAR polarity domains involves actomyosin cortical flows that transport PAR proteins [6, 8–11]. In addition PAR proteins regulate the actomyosin cortex [8, 12–16], implying mechanochemical feedback [17]. Two centrosomal polarity triggers act as guiding cues for the polarization process [1–3]. First, centrosomal microtubules protect PAR-2 from PKC-3-mediated antagonism [5]. Second, contractility in the actomyosin cortex is increased via RhoA activation [18], and a local down-regulation of non-muscle myosin II (NMY-2, referred to as myosin) at the posterior pole [19] initiates cortical flows [8, 20]. The relationship between guiding cues and feedback in PAR polarity establishment remains unclear. To address this issue, we first focus on feedback and later shift our attention to the guiding cues and their relation to the mechanisms of feedback.

Previous work has investigated antagonistic feedback between the two PAR species [4, 6, 21]. We set out to characterize mechanochemical feedback from PAR proteins onto actomyosin contractility. Cortical myosin is regulated by PAR domains [8, 12–16], but the strength of this regulation in terms of changes of myosin association and dissociation rates remains unknown. Fluorescence Recovery After Photobleaching (FRAP) is a technique for determining dissociation rates at steady-state [22, 23] (Supplementary Fig. 1, Supplementary Discussion 1.2). Performing FRAP during maintenance where myosin appears to reach a steady state (Supplementary Fig. 2a,c, Supplementary Discussion 1.2), we found that the rate of NMY-2 dissociation from the cortex is about two-fold higher in the posterior compared to the anterior PAR domain (posterior, k_{diss}= 0.14 $\pm$ 0.01 s^{-1}; anterior, k_{diss}= 0.072 $\pm$ 0.009 s^{-1}) (Fig. 1b). The spontaneous dissociation rate of myosin in anterior during maintenance is similar to the one reported during cortical flows, as measured via co-moving mass-balance imaging (COMBI; [24]). This indicates that myosin reaction kinetics do not change much over these stages of the cell cycle. We next determined the rate of NMY-2 association to the cortex by considering that the steady-state surface concentration of NMY-2 is set by the ratio of this association rate and the dissociation rate from the cortex. To this end, we developed a fluorescence-based image quantification technique (MACE: Membrane-Associated Concentration Evaluation) that determines the spatiotemporal concentration fields of

labeled proteins at the cell surface (Fig. 1a, see also [25]). We find that the rates of association of NMY-2 to the cortex are similar in both PAR domains (anterior: $k_{\mathrm{on}} = 0.19 \pm 0.03\ \mu\mathrm{m\,s}^{-1}$, posterior: $k_{\mathrm{on}} = 0.21 \pm 0.03\ \mu\mathrm{m\,s}^{-1}$) (Fig. 1d), indicating that NMY-2 association to the cortex is independent of PARs. However, changing the local PAR state of the cortex via RNAi changes the local NMY-2 dissociation rate (Fig. 1b, Supplementary Fig. 2k), indicating that the PAR domain state controls NMY-2 dissociation from the cortex. We next asked if the posterior or the anterior PAR complex regulates the NMY-2 dissociation rate. To this end, we measured the NMY-2 dissociation rate during *par-2* and *par-6* double-RNAi (Supplementary Fig. 2j). Under this condition, the NMY-2 dissociation rate is not significantly different from the one measured in the posterior domain of unperturbed embryos (Fig. 1b), indicating that the anterior PAR complex is the dominant regulator of the myosin dissociation rate [26]. Indeed, by combining FRAP data with MACE analysis we find that the dissociation rate k_{diss} of NMY-2 decreases with increasing PAR-6 concentration approximately as $k_{\mathrm{diss}} = (k_{\mathrm{off},M} + k_{AM}A)$, where $k_{\mathrm{off},M}$ is the spontaneous dissociation rate of NMY-2 in the absence of PARs, A is the anterior PAR-6 concentration and k_{AM} is a coupling coefficient ($k_{AM} = (-2.0 \pm 0.7) \cdot 10^{-3}\ \mu\mathrm{m}^2\,\mathrm{s}^{-1}$; Fig. 1c, Supplementary Fig. 2k). Thus, anterior PAR complexes control the amount of cortical myosin by regulating its dissociation rate. This gives rise to mechanochemical feedback since controlling myosin levels controls actomyosin flows, and thus flow-based PAR complex transport [6, 8–11, 20].

Feedback structures allow non-equilibrium systems to spontaneously break symmetry and form self-organized patterns [27–29]. However, external signals can couple to self-organized Turing-like systems, for breaking symmetry and for guiding mechanisms of pattern formation to realize appropriate spatiotemporal profiles of constituents [30–37]. We next set out to investigate the relationship between feedback and guidance in PAR polarization, and develop a theory of guided mechanochemical self-organization where PAR distributions, myosin distribution and cortical flow pattern are all interdependent and respond to guiding cues. We aimed for a description that is simple enough to capture all relevant processes, but still contains enough detail to be of predictive power. Two feedback mechanisms are included: antagonism between anterior and posterior PAR proteins is captured by a mass-conserved Turing-like system [6, 38, 39], and mechanochemical feedback is captured by coupling the Turing-like system to an active fluid to describe the mechanics of the actomyosin cortex [20, 40]. In addition, two guiding cues modify PAR and myosin concentration fields over space and time to steer the polarization process. We write reaction-advection-diffusion equations for the cell surface concentration fields of PAR-2 (P), PAR-6 (A),

and myosin (M) as representatives for the posterior PAR complex, the anterior PAR complex, and the contractile actomyosin cortex, respectively (Fig. 2a). We consider azimuthal symmetry around the long axis of the egg, and pursue a 1D description with periodic boundary conditions, where the spatial coordinate x denotes the distance along the surface to the posterior pole ($-L/2 < x < L/2$, with L denoting the circumference of the embryo; Fig. 1a).

$$\partial_t A = \underbrace{-\partial_x(v\,A)}_{\text{advective transport}} + \underbrace{D_A\,\partial_x^2 A}_{\text{diffusion}} + \underbrace{\frac{k_{\text{on},A}}{1+k_{AP}P^{\alpha}}A_{\text{cyto}} - k_{\text{off},A}A}_{\text{biochemical interactions}}, \tag{1}$$

$$\partial_t P = \underbrace{-\partial_x(v\,P)}_{\text{advective transport}} + \underbrace{D_P\,\partial_x^2 P}_{\text{diffusion}} + \underbrace{k_{\text{on},P}P_{\text{cyto}} - k_{\text{off},P}P - k_{PA}A^{\beta}P + c_{\text{P}}(x,t)}_{\text{biochemical interactions}}, \tag{2}$$

$$\partial_t M = \underbrace{-\partial_x(v\,M)}_{\text{advective transport}} + \underbrace{D_M\,\partial_x^2 M}_{\text{diffusion}} + \underbrace{k_{\text{on},M}M_{\text{cyto}} - k_{\text{off},M}M + k_{AM}AM + c_{\text{M1}}(x,t)}_{\text{biochemical interactions}}, \tag{3}$$

Here, v denotes the cortical flow velocity, and D_A, D_P, and D_M describe the respective diffusion coefficients of the three species in the cortex-associated state. Antagonistic feedback between the two PAR species is controlled by k_{AP} and k_{PA} [6, 21], and mechanochemical feedback arises from the regulation of the myosin dissociation rate by aPARs via k_{AM} (Fig. 1c). Note that our experimental measurement of the PAR-6 dependent dissociation rate of myosin does not rule out additional regulatory interactions between the PAR proteins and the actomyosin cortex. Spontaneous binding and unbinding rates of $S \in \{A,P,M\}$ are denoted by $k_{\text{on},S}$ and $k_{\text{off},S}$, respectively. Oligomerization states of aPAR and pPAR complexes [9–11, 41] are captured via effective coefficients, nonlinear interactions and the stoichiometric coefficients α, β [6]. All species obey mass-conservation, and cytoplasmic concentrations A_{cyto}, P_{cyto}, and M_{cyto} are determined by $S_{\text{cyto}} = \rho_S - \frac{\psi}{L}\int_{-L/2}^{L/2} S(x,t)dx$, where $\rho_S V$ is the total number of molecules of type $S \in \{A,P,M\}$. Cytoplasmic volume is denoted by V, and ψ is the surface-to-volume ratio. Finally, we consider two guiding cues, the PAR-2 stabilization cue c_{P} (reducing the inhibition of aPARs onto pPARs) and the actomyosin cue. The latter consists of two cue components, a myosin removal component c_{M1} (increasing the spontaneous NMY-2 dissociation rate), and a contractility component c_{M2} (modifying overall contractility):

$$c_{\text{P}}(x,t) = k_{PA}A^{\beta}P\,\kappa_P F_P(x) f_P(t), \tag{4}$$

$$c_{\text{M1}}(x,t) = -k_{\text{off},M}M\,\kappa_M F_M(x) f_M(t)\,, \quad c_{\text{M2}}(t) = f_C(t). \tag{5}$$

Here $F_P(x)$ and $F_M(x)$ characterize the impact of the respective cues in a region around the posterior pole with a gaussian profile, while $f_P(t)$, $f_M(t)$, and $f_C(t)$ characterize the respective time-dependent behaviors of cues and cue components, smoothly transitioning between off- and on-states (Supplementary Equations (28-32), Supplementary Fig. 6). κ_P and κ_M scale the amplitudes of the respective cues. Contractility C depends on myosin concentration M, and gradients in C drive cortical flows, which are resisted by an effective cortex viscosity η and frictional drag γ with membrane and cytoplasm according to [20]:

$$\ell^2 \partial_x^2 v - v = -\frac{C_*}{\gamma}\,\partial_x C, \qquad C = c_{\mathrm{M2}}(t)\,\frac{M}{M+M_*}, \tag{6}$$

with $\ell = \sqrt{\eta/\gamma}$ a hydrodynamic length-scale [42], C_* a proportionality constant, and M_* a contractility saturation constant. Supplementary Fig. 12 provides an analysis how sensitive this theory is to changes in each of the 28 parameters. Seven of these parameters are known (Supplementary Table 2, [6, 23, 42, 43]). In this study, we directly measured ten more parameters (Supplementary Tables 2,3, Fig. 1c,d, Supplementary Fig. 3-6). We determined the remaining eleven parameters by a systematic parameter inference procedure, where numerical solutions are compared to the experimental dynamics of Figure 2 (Supplementary Fig. 13-15, see and Supplementary Information, section 2.6 for details), With this approach, we i) characterized spatiotemporal activity profiles of guiding cues, and ii) calibrated our theory by determining all interactions and parameters of the PAR - actomyosin patterning system.

We first determined the spatiotemporal activity profiles of guiding cues, by fitting measured distributions of aPARs, pPARs, and myosin together with the cortical flow to our theoretical description (Supplementary Information, section 2.6). For each cue we utilized RNAi to perform our analysis in a reduced system, where a guiding cue is singled out. First, we isolated the PAR-2 stabilization cue (c_P, Fig. 2a) by suppressing cortical flows via RNAi of the regulatory myosin light chain *mlc-4*, which inhibits advective transport of PAR proteins (Supplementary Fig. 7a,b). Using MACE, we showed that PAR domains still form under *mlc-4* RNAi (Fig. 2b), consistent with previous work [5, 15]. Here, the spatiotemporal dynamics of PAR proteins (Fig. 2b) are driven by the PAR-2 stabilization cue and PAR-reaction-chemistry-dependent feedback alone. Applying a systematic parameter inference procedure, we quantified four kinetic parameters of the PAR interaction network (the antagonistic interaction strengths k_{AP}, k_{PA} and the association rates $k_{\mathrm{on},A}$,

$k_{\mathrm{on},P}$; eqs. 1,2,5, Supplementary Information, section 2.6, Supplementary Tables 1,2) together with the spatiotemporal activity profile of the PAR-2 stabilization cue onto the PAR system (Fig. 2d, Supplementary Information, section 2.4-2.6). With this, we can quantitatively account for the measured PAR distributions over the entire polarization process under *mlc-4* RNAi (Fig. 2c, Supplementary Video 1). We find that the PAR-2 stabilization cue is turned on with a characteristic time scale of 74 ± 4 seconds, acts over almost half the surface of the embryo (width: 57.2 ± 0.3 µm) and protects approximately 95% of the PAR-2 proteins from aPAR-dependent antagonism [5] near the posterior pole (Fig. 2d, Supplementary Table 2). To conclude, we have quantified the spatiotemporal activity profile of the PAR-2 stabilization cue.

Second, we characterized the actomyosin guiding cue, which triggers cortical flows. This cue consists of two components: First, a contractility component initially increases myosin activity throughout the entire cortex in preparation for polarity establishment, and later globally down-regulates myosin activity when PAR domains are established [18]. Second, a myosin removal component locally removes myosin in the vicinity of the centrosome at the posterior pole for a transient period of time, to generate a contractile imbalance that initiates cortical flows [19]. Since both the PAR system (Fig. 1c) and this two-component actomyosin guiding cue impact on myosin, we set out to render the PAR system ineffective in order to isolate the actomyosin cue. Double-RNAi of *par-2* and *par-6* reduced the PAR-2 and PAR-6 amounts to a degree that the regulation of PARs on myosin is negligible (see Supplementary Discussion, section 1.1 and Supplementary Fig. 10,11). An active-fluid description of actomyosin (eqs. 3,4,6; Supplementary Table 1) together with a systematic parameter inference procedure (Supplementary Information, section 2.4-2.6) allowed us to quantify two physical parameters of the actomyosin system (C_* and M_*, which control the relation between myosin concentrations and contractility, Supplementary Information, section 2.6, Supplementary Tables 1,2) together with the activity profile of both components of the actomyosin cue. With this, our theory describes at a quantitative level the measured NMY-2 distribution and cortical flow field under double RNAi of *par-2* and *par-6* (Fig. 2f,h, Supplementary Video 2). We find that the myosin removal component of the actomyosin cue down-regulates NMY-2 by increasing its dissociation rate by a factor of about 6 in a restricted region close to the posterior pole (width: 31.7 ± 1.2 µm) for a time of 204 ± 10 s (Fig. 2i) [19]. The contractility component of the actomyosin cue is active even before polarity initiation at t = 0 s, and its time of inactivation appears to coincide with the inactivation of the myosin removal component (Fig. 2j, Supplementary Fig. 5). To summarize, we have inactivated mechanochemical feedback to isolate

both the PAR and the actomyosin subsystems in order to i) determine the strength of all unknown interactions in our theoretical description and ii) quantify the spatiotemporal profile of both guiding cues.

We next tested if our theory correctly describes how feedback structures and guiding cues together orchestrate PAR polarity establishment. To this end, we set out to predict the spatiotemporal evolution of PAR polarization in the full system and in presence of mechanochemical feedback (Fig. 1c), starting from the unpolarized state that is perturbed by both cues (Fig. 2). We investigated two conditions, unperturbed PAR polarity establishment (Fig. 3h-j) as well as PAR polarity establishment for a PAR-2 mutant with an inactive PAR-2 stabilization cue [5] (referred to as PAR-2 MT-; Fig. 3a-c). We obtained a theoretical prediction for both conditions by numerically solving equations 1-6 (Supplementary Table 1) using above-determined parameter values (Supplementary Tables 2,3) and setting the strength of the PAR-2 stabilization cue to zero for the PAR-2 MT- condition. We find good agreement between theoretical predictions and experimental data for all fields measured (Fig. 3d-g, k-n, Supplementary Videos 3,4). PAR-2 dynamics are captured better for PAR-2 MT- as compared to the unperturbed case, which is indicative of an alteration of the spatiotemporal dynamics of the PAR-2 stabilization cue between the unperturbed and the *mlc-4* RNAi condition we have not considered (Supplementary Fig. 9, Supplementary Video 5). Hence, we are able to account for the spatiotemporal dynamics of the full PAR - actomyosin system, and we conclude that our theory appropriately captures both guidance and feedback.

We next set out to investigating the relationship between feedback and guidance. For this, we studied the temporal evolution of the full system in terms of the total numbers of proteins of PAR-2, PAR-6, and NMY-2 associated to the cortex, respectively. We set out to reveal in our theory which interactions drive the system from the unpolarized to the polarized state, differentiating between terms associated to guidance and terms associated to feedback (see Methods; Fig. 2a). We make two observations: first, instantaneously setting to zero all terms associated with guidance prior to approximately 60 s results in the system returning back to the initial and unpolarized state, while the system continues to progress towards the polarized state when these terms are set to zero beyond this point in time (Supplementary Fig. 8). Second, the contribution of guidance terms to the time evolution of the trajectory switches from assisting to impeding (Fig. 4a, light blue arrowheads; also see Methods) at about 260 s. Together, this reveals three phases of polarity establishment: guiding cues are required in the initial phase up to 60 s (transition point, Fig. 4a,e, Supplementary Fig. 8), guiding cues are no longer required but assist the polarization process in a

second phase up to 260 s (guidance release, Fig. 4a,e), and guiding cues impedes the process and self-organization takes over in determining the systems' dynamics in the final phase (Fig. 4a,e). Our analysis indicates that two features are important for achieving controllability and robustness. First, feedback remains subcritical throughout to avoid unstable behaviour and spontaneous pattern formation. Consistent with this, *C. elegans* zygotes have not been observed to polarize in the absence of cues [1, 5, 44, 45], but how far the PAR - actomyosin patterning system is placed away from a mechanochemical instability is not known [24, 40]. We tested for subcritical feedback in our theory by performing a linear stability analysis of the homogeneous state. We find that the system is poised far away from the unstable regime (Fig. 4b, white region), which allows for control of pattern formation since the system will only polarize in response to guiding cues. Second, to achieve robustness guiding cues need to be strong enough and active long enough to drive the system significantly beyond the 'barrier to polarization' (i.e. the transition point at 60 s, Fig. 4a). For example, our theoretical analysis suggests that the actomyosin guiding cue is not strong enough to to drive the system beyond the transition state when contractility drops below a critical threshold (Fig. 4b, grey region), and predicts a critical flow speed of 3.7 µm min^{-1} required for polarization (Fig. 5b). To test this, we isolated the actomyosin cue (PAR-2 MT- mutant condition, Fig. 5a) and gradually reduced cortical flow speeds by performing a series of milder-to-stronger *mlc-4* RNAi experiments. Consistent with our prediction, embryos failed to polarize when cortical flow speeds dropped to about half the flow speed of unperturbed embryos (6.9 ± 0.3 μm min^{-1}; Fig. 5b). Hence, the actomyosin cue generates cortical flows that are approximately twice the critical speed required for successful polarization, which provides robustness. Next, we experimentally investigated how long the PAR-2 stabilization cue needs to be active to achieve polarization. We laser-ablated centrosomes at different times ([45]; Fig. 5c), recorded the spatial profiles of the nucleated PAR-2 domain at the moment of ablation and for each experiment, and assessed if embryos continued to evolve towards the polarized state afterwards, or returned back to the unpolarized state (Fig. 5c, see Methods). We found that the minimal PAR-2 domain required for polarization in the experiment (Fig. 5d) was similar to the PAR-2 domain at the transition point as predicted from theory (Fig. 5d, Fig. 4a). Notably, while approximately 70,000 PAR-2 proteins are cortex-associated at the time of guidance release (t=260 s, Fig. 4a), only about 10,000 PAR-2 proteins are required to reach the transition point that needs to be passed for achieving polarization (Fig. 5d). Hence, the PAR-2 stabilization cues drives the system far beyond the 'barrier to polarization', which provides robustness.

A fundamental challenge for patterning system is that they typically involve unstable behaviors that are hard to control. Our analysis indicates that polarity pattern formation in *C. elegans* avoids local instabilities. Feedback structures are subcritical but generate basins of attraction around (at least) two states, one corresponding to the unpatterned and one to the patterned state (Fig. 4c). Guiding cues drive the system away from the unpatterned state (Fig. 4d) and beyond its basin of attraction, and into the vicinity of the patterned state. Finally, self-organization can take over in shaping the time evolution of the system near the patterned state (Fig. 4e). Thus, guiding cues are active for a significant fraction of the trajectory, rendering PAR polarization deterministic and likely conferring robustness. Note that guiding cues can be either temporary and functioning only in triggering pattern formation (as is the case for the actomyosin cue, Fig. 2i, j) or permanent and with a possible role in shaping the final patterned state (PAR-2 stabilization cue, Fig. 2d). Interestingly, two guiding cues shape the self-organized dynamics of the system, and these dynamics are generated by two distinct feedback structures (PAR antagonism, mechanochemical feedback). We speculate that combining several feedback structures and controlling each one with its own guiding cue is a general mechanism for providing specificity and robustness in controlled biological pattern formation.

[1] Fumio Motegi, Geraldine Seydoux. The PAR network: redundancy and robustness in a symmetry-breaking system. *Philosophical Transactions of the Royal Society B: Biological Sciences*, 368(1629), (2013).

[2] Carsten Hoege, Anthony A. Hyman. Principles of PAR polarity in Caenorhabditis elegans embryos. *Nature Reviews Molecular Cell Biology*, 14(5):315–322, (2013).

[3] Charles F. Lang, Edwin Munro. The PAR proteins: from molecular circuits to dynamic self-stabilizing cell polarity. *Development*, 144(19):3405–3416, (2017).

[4] Bob Goldstein, Ian G. Macara. The PAR proteins: Fundamental players in animal cell polarization. *Developmental Cell*, 13(5):609–622, (2007).

[5] Fumio Motegi, Seth Zonies, Yingsong Hao, Adrian A. Cuenca, Erik Griffin, Geraldine Seydoux. Microtubules induce self-organization of polarized PAR domains in Caenorhabditis elegans zygotes. *Nature Cell Biology*, 13(11):1361–1367, (2011).

[6] Nathan W. Goehring, Philipp Khuc Trong, Justin S. Bois, Debanjan Chowdhury, Ernesto M. Nicola, Anthony A. Hyman, Stephan W. Grill. Polarization of PAR Proteins by Advective Triggering of a Pattern-Forming System. *Science*, 334(6059):1137–1141, (2011).

[7] Philipp Khuc Trong, Ernesto M. Nicola, Nathan W. Goehring, K. Vijay Kumar, Stephan W. Grill. Parameter-space topology of models for cell polarity. *New Journal Of Physics*, 16, (2014).

[8] Edwin Munro, Jeremy Nance, James R. Priess. Cortical flows powered by asymmetrical contraction transport PAR proteins to establish and maintain anterior-posterior polarity in the early C. elegans embryo. *Developmental Cell*, 7(3):413–424, (2004).

[9] Shyi-Chyi Wang, Tricia Yu Feng Low, Yukako Nishimura, Laurent Gole, Weimiao Yu, Fumio Motegi. Cortical forces and CDC-42 control clustering of PAR proteins for Caenorhabditis elegans embryonic polarization. *Nature Cell Biology*, 19(8):988–995, (2017).

[10] Josana Rodriguez, Florent Peglion, Jack Martin, Lars Hubatsch, Jacob Reich, Nisha Hirani, Alicia G Gubieda, Jon Roffey, Artur Ribeiro Fernandes, Daniel St Johnston, Julie Ahringer, Nathan W Goehring. aPKC Cycles between Functionally Distinct PAR Protein Assemblies to Drive Cell Polarity. *Developmental Cell*, 42:400–415, (2017).

[11] Daniel J. Dickinson, Francoise Schwager, Lionel Pintard, Monica Gotta, Bob Goldstein. A Single-Cell Biochemistry Approach Reveals PAR Complex Dynamics during Cell Polarization. *Developmental*

Cell, 42(4):416–434, (2017).

[12] Stephan Q. Schneider, Bruce Bowerman. Cell polarity and the cytoskeleton in the Caenorhabditis elegans zygote. *Annual Review of Genetics*, 37:221–249, (2003).

[13] Rebecca J. Cheeks, Julie C. Canman, Willow N. Gabriel, Nicole Meyer, Susan Strome, Bob Goldstein. C. elegans PAR proteins function by mobilizing and stabilizing asymmetrically localized protein complexes. *Current Biology*, 14(10):851–862, (2004).

[14] Alexander Beatty, Diane G. Morton, Kenneth Kemphues. PAR-2, LGL-1 and the CDC-42 GAP CHIN-1 act in distinct pathways to maintain polarity in the C. elegans embryo. *Development*, 140(9):2005–2014, (2013).

[15] Seth Zonies, Fumio Motegi, Yingsong Hao, Geraldine Seydoux. Symmetry breaking and polarization of the C. elegans zygote by the polarity protein PAR-2. *Development*, 137(10):1669–1677, (2010).

[16] Jeremy Nance, Jennifer A. Zallen. Elaborating polarity: PAR proteins and the cytoskeleton. *Development*, 138(5):799–809, (2011).

[17] Peter Gross, K. Vijay Kumar, Stephan W. Grill. How active mechanics and regulatory biochemistry combine to form patterns in development. *Annual Review of Biophysics*, 46(1):337–356, (2017).

[18] Yu Chung Tse, Michael Werner, Katrina M. Longhini, Jean-Claude Labbe, Bob Goldstein, Michael Glotzer. RhoA activation during polarization and cytokinesis of the early Caenorhabditis elegans embryo is differentially dependent on NOP-1 and CYK-4. *Molecular Biology of the Cell*, 23(20):4020–4031, (2012).

[19] Fumio Motegi, Asako Sugimoto. Sequential functioning of the ECT-2 RhoGEF, RHO-1 and CDC-42 establishes cell polarity in Caenorhabditis elegans embryos. *Nature Cell Biology*, 8(9):978–985, (2006).

[20] Mirjam Mayer, Martin Depken, Justin S. Bois, Frank Jülicher, Stephan W. Grill. Anisotropies in cortical tension reveal the physical basis of polarizing cortical flows. *Nature*, 467(7315):617–621, (2010).

[21] Anne Sailer, Alexander Anneken, Younan Li, Sam Lee, Edwin Munro. Dynamic Opposition of Clustered Proteins Stabilizes Cortical Polarity in the C. elegans Zygote. *Developmental Cell*, 35(1):131–142, (2015).

[22] Nathan W. Goehring, Debanjan Chowdhury, Anthony A. Hyman, Stephan W. Grill. FRAP Analysis of Membrane-Associated Proteins: Lateral Diffusion and Membrane-Cytoplasmic Exchange. *Biophysical Journal*, 99(8):2443–2452, (2010).

[23] Nathan W. Goehring, Carsten Hoege, Stephan W. Grill, Anthony A. Hyman. PAR proteins diffuse freely across the anterior-posterior boundary in polarized C. elegans embryos. *Journal of Cell Biology*, 193(3):583–594, (2011).

[24] Masatoshi Nishikawa, Sundar Ram Naganathan, Frank Jülicher, Stephan W. Grill. Controlling contractile instabilities in the actomyosin cortex. *eLife*, 6, (2017).

[25] JQ Wu, TD Pollard. Counting cytokinesis proteins globally and locally in fission yeast. *Science*, 310(5746):310–314, (2005).

[26] Daryl J. V. David, Alisa Tishkina, Tony J. C. Harris. The PAR complex regulates pulsed actomyosin contractions during amnioserosa apical constriction in Drosophila. *Development*, 137(10):1645–1655, (2010).

[27] Alan M Turing. The Chemical Basis of Morphogenesis. *Philosophical Transactions of the Royal Society of London Series B-Biological Sciences*, 237(641):37–72, (1952).

[28] Shigeru Kondo, Takashi Miura. Reaction-Diffusion Model as a Framework for Understanding Biological Pattern Formation. *Science*, 329(5999):1616–1620, (2010).

[29] Luciano Marcon, James Sharpe. Turing patterns in development: what about the horse part? *Current Opinion in Genetics & Development*, 22(6):578–584, (2012).

[30] Alexander S. Mikhailov, Kenneth Showalter. Control of waves, patterns and turbulence in chemical systems. *Physics Reports-Review Section of Physics Letters*, 425(2-3):79–194, (2006).

[31] Mikhail Prokopenko. Guided self-organization. *HFSP Journal*, 3(5):287–289, (2009).

[32] Mikiya Otsuji, Shuji Ishihara, Carl Co, Kozo Kaibuchi, Atsushi Mochizuki, Shinya Kuroda. A mass conserved reaction-diffusion system captures properties of cell polarity. *PLOS Computational Biology*, 3(6):1040–1054, (2007).

[33] Alexandra Jilkine, Leah Edelstein-Keshet. A Comparison of Mathematical Models for Polarization of Single Eukaryotic Cells in Response to Guided Cues. *PLOS Computational Biology*, 7(4), (2011).

[34] Fabai Wu, Jacob Halatek, Matthias Reiter, Enzo Kingma, Erwin Frey, Cees Dekker. Multistability and dynamic transitions of intracellular Min protein patterns. *Molecular Systems Biology*, 12(6), (2016).

[35] J. Raspopovic, L. Marcon, L. Russo, J. Sharpe. Digit patterning is controlled by a bmp-sox9-wnt turing network modulated by morphogen gradients. *Science*, 345:566–570, (2014).

[36] Francis Corson, Lydie Couturier, Herve Rouault, Khalil Mazouni, Francois Schweisguth. Self-organized Notch dynamics generate stereotyped sensory organ patterns in Drosophila. *Science*, 356(6337):501–508, (2017).

[37] Marcin Zagorski, Yoji Tabata, Nathalie Brandenberg, Matthias P. Lutolf, Gašper Tkačik, Tobias Bollenbach, James Briscoe, Anna Kicheva. Decoding of position in the developing neural tube from antiparallel morphogen gradients. *Science*, 356(6345):1379–1383, (2017).

[38] Sungrim Seirin Lee, Tatsuo Shibata. Self-organization and advective transport in the cell polarity formation for asymmetric cell division. *Journal of Theoretical Biology*, 382:1–14, (2015).

[39] Jacob Halatek, Erwin Frey. Rethinking pattern formation in reaction–diffusion systems. *Nature Physics*, 14:507–514, (2018).

[40] Justin S. Bois, Frank Jülicher, Stephan W. Grill. Pattern Formation in Active Fluids. *Physical Review Letters*, 106(2), (2011).

[41] Yukinobu Arata, Michio Hiroshima, Chan-Gi Pack, Ravikrishna Ramanujam, Fumio Motegi, Kenichi Nakazato, Yuki Shindo, Paul W Wiseman, Hitoshi Sawa, Tetsuya J Kobayashi, Hugo B Brandão, Tatsuo Shibata, Yasushi Sako. Cortical Polarity of the RING Protein PAR-2 Is Maintained by Exchange Rate Kinetics at the Cortical-Cytoplasmic Boundary. *Cell Reports*, 16(8):2156–2168, (2016).

[42] Arnab Saha, Masatoshi Nishikawa, Martin Behrndt, Carl-Philipp Heisenberg, Frank Jülicher, Stephan W. Grill. Determining Physical Properties of the Cell Cortex. *Biophysical Journal*, 110(6):1421–1429, (2016).

[43] Francois B. Robin, William M. McFadden, Baixue Yao, Edwin M. Munro. Single-molecule analysis of cell surface dynamics in Caenorhabditis elegans embryos. *Nature Methods*, 11(6):677–682, (2014).

[44] Edwin Munro, Bruce Bowerman. Cellular Symmetry Breaking during *Caenorhabditis elegans* Development. *Cold Spring Harbor Perspectives in Biology*, 1(4), (2009).

[45] Carrie R. Cowan, Anthony A. Hyman. Centrosomes direct cell polarity independently of microtubule assembly in C. elegans embryos. *Nature*, 431(7004):92–96, (2004).

[46] RS Kamath, J Ahringer. Genome-wide RNAi screening in Caenorhabditis elegans. *Methods*, 30(4):313–321, (2003).

[47] Jakub Sedzinski, Mate Biro, Annelie Oswald, Jean-Yves Tinevez, Guillaume Salbreux, Ewa Paluch. Polar actomyosin contractility destabilizes the position of the cytokinetic furrow. *Nature*, 476(7361):462–466, (2011).

[48] Simon Blanchoud, Coralie Busso, Felix Naef, Pierre Goenczy. Quantitative Analysis and Modeling Probe Polarity Establishment in C. elegans Embryos. *Biophysical Journal*, 108(4):799–809, (2015).

[49] S. Ruettinger, V. Buschmann, B. Kraemer, R. Erdmann, R. Macdonald, F. Koberling. Comparison and accuracy of methods to determine the confocal volume for quantitative fluorescence correlation

spectroscopy. *Journal of Microscopy*, 232(2):343–352, (2008).

[50] Khuloud Jaqaman, Dinah Loerke, Marcel Mettlen, Hirotaka Kuwata, Sergio Grinstein, Sandra L. Schmid, Gaudenz Danuser. Robust single-particle tracking in live-cell time-lapse sequences. *Nature Methods*, 5(8):695–702, (2008).

[51] Thielicke, William, Stamhuis, Eize J . PIVlab - Towards User-friendly, Affordable and Accurate Digital Particle Image Velocimetry in MATLAB. *Journal of Open Research Software*, 2(1), (2014).

FIG. 1. **Mechanochemical feedback in PAR polarity establishment.** **a**, Example of PAR and myosin protein concentration and velocity fields obtained at a single time point during polarity establishment from confocal medial sections using MACE (4 minutes after flow onset; blue, PAR-2::GFP representing pPARs; red, PAR-6::mCherry representing aPARs; grey, NMY-2::GFP; see Methods). Scale bar, 5 μm. A and P denote the anterior and posterior, respectively. x indicates the position along the circumference, with the posterior pole at x = 0. **b**, Average NMY-2 dissociation rates as measured by FRAP for unperturbed, *par-2*, *par-6* and *par-2* / *par-6* double RNAi embryos as a function of position and cortical PAR state (see schematics at the bottom); see Supplementary Fig. 2d-g for statistics. **c**, NMY-2 dissociation rates as a function of PAR-6 concentration. Solid line represents a linear fit with slope k_{AM} = -0.002 ± 0.0007 $\mu m^2\, s^{-1}$ and intercept $k_{off,M}$ = 0.117 ± 0.009 s^{-1}. Due to uncertainties in the determining the PAR-6 concentration, condition [6] (*par-2* RNAi, posterior side) was not included (Supplementary Fig. 2h). **d**, NMY-2 association rates as a function of position and cortical PAR state (see schematics at the bottom). Error bars are standard error of the mean.

FIG. 2. **Isolating both guiding cues by RNAi and determining their spatiotemporal profiles.** **a**, M, A, P, represent myosin, aPARs and pPARs, respectively. These are located either in the cytoplasm or at the cortex where they are subjected to lateral diffusion and advective transport by cortical flow. We consider spontaneous association and dissociation to and from the cortex, mutual inhibitory interactions between the aPARs and the pPARs in the cortex-associated state, as well as an aPAR-dependent regulation of cortical myosin concentration. Two polarity triggers steer the polarization process, one impacts on the cortical pPAR concentration (c_P: PAR-2-stabilization cue, see text for details), and one impacts on the actomyosin cortex with two components (c_{M1}: myosin removal cue component, c_{M2}: contractility cue component, see text for details). **b**, Average spatiotemporal distributions of aPARs (PAR-6::mCherry) and pPARs (PAR-2::GFP) over the time-course of polarity establishment obtained by MACE and with *mlc-4* RNAi to inhibit cortical flows (N=8 embryos, Supplementary Fig. 7b). **c**, Best fits from theory (displayed at t = 50 s, 200 s and 450 s; solid lines; Supplementary Video 1) to MACE data (dots, shaded regions represent standard error of the mean) are used to determine **d**, the spatiotemporal profile of the PAR-2 stabilization cue c_P, which reduces the anterior PAR complex-dependent inhibition of PAR-2. **e**, Average spatiotemporal profile of myosin (NMY-2::GFP) during *par-2* and *par-6* double RNAi to inactivate the PAR system (N = 8 embryos, Supplementary Discussion and Supplementary Fig. 10,11). **g**, Corresponding average myosin flow field (N = 10 embryos, see Methods). **f,h**, Best fits from theory (displayed at t = 50 s, 200 s and 450 s; Supplementary Video 2) to MACE data (dots, shaded regions represent standard error of the mean) are used to determine **i**, the spatiotemporal profile of the myosin removal cue component c_{M1}, which increases the myosin dissociation rate, and **j**, the spatiotemporal profile of the actomyosin contractility cue component c_{M2}, which controls the mechanical contractility of the cortex.

FIG. 3. **Predicting PAR and myosin dynamics in the presence of guiding cues and feedback structures.** **a-c**, Average spatiotemporal distributions of **a**, aPARs (PAR-6::mCherry) and pPARs (PAR-2::GFP) (both N = 9 embryos), **b**, myosin (NMY-2::mKate2; N = 6 embryos) together with **c**, the myosin flow field (N = 9 embryos) during polarity establishment for the PAR-2 MT- mutant. **d-f**, Comparison of MACE data for the PAR-2 MT- mutant (dots, shaded regions represent standard error of the mean) to theory predictions (displayed at t = 50 s, 200 s and 450 s; see Supplementary Video 3). **h-j**, Average spatiotemporal distributions of **h**, aPARs (PAR-6::mCherry) and pPARs (PAR-2::GFP) (both N = 6 embryos), **i**, myosin (NMY-2::GFP; N = 8 embryos) together with **j**, the myosin flow field (N = 12 embryos) during polarity establishment of the unperturbed condition. **k-m**, Comparison of MACE data for the unperturbed condition (dots, shaded regions represent standard error of the mean) to theory predictions (displayed at t = 50 s, 200 s and 450 s; solid lines); see Supplementary Video 4. **g,n**, Comparison of the measured and predicted PAR-2 domain width for the unperturbed condition (**n**) and the PAR-2 MT- mutant (**g**). Error bars are standard error of the mean.

FIG. 4. **Handover from cue-driven to mechanochemically self-organized dynamics.** **a**, Evolution of the total numbers of cortical PAR-2, PAR-6 and NMY-2 with both cues active, as determined by numerical evaluation of eqs. 1-6. Black arrows denote an increase in protein numbers by 10^4. Arrowheads indicate projections of time-rate changes induced by guidance (dark blue) and self-organization (light blue) onto the tangent of the trajectory (see Methods). Guidance release (red point at T $\approx$ 260 s) occurs when the guiding cue component of the evolution dynamics switches from assisting (i.e. pulling forwards along the trajectory) to impeding (pulling backwards along the trajectory). Guiding cues need to be active only up to the transition point at T $\approx$ 60 s (green dot) to achieve polarization (Supplementary Fig. 8). **b**, Stability diagram of the homogeneous aPAR-high state as a function of both the contractility strength C_*/γ and the aPAR-myosin coupling coefficient k_{AM}. The system is unable to polarize in response to the actomyosin cue (c_{M1} together with c_{M2}) in the grey region, polarizes in response to the actomyosin cue in the yellow region, and undergoes spontaneous pattern formation in absence of any cue in the white region. **c-e**, Schematic of the mechanisms of pattern formation via guided mechanochemical self-organization.

FIG. 5. **Robust PAR polarization breaks down close to the transition point.** **a**, Two individual PAR-2 MT- mutant embryos that were exposed to different *mlc-4* RNAi feeding times, resulting in reduced peak cortical flow velocities v (Supplementary Fig. 7c). left: no PAR domains, right: PAR domains form. Scale bar, 5 µm. **b**, Cortical flow velocities for 28 zygotes, exposed to weaker-to-stronger *mlc-4* RNAi. Upper row and yellow circles, embryos successfully polarized (N=15); bottom row and grey diamonds, embryos failed to polarize (N=13). Green vertical line indicates the theoretically predicted critical velocity ($v_{critical}$) required for polarization by the actomyosin cue (c_{M1} together with c_{M2}). The peak cortical flow velocity of unperturbed zygotes (mean $\pm$ SEM) is also indicated. **c**, Inhibition of the centrosomal polarity trigger via laser-ablation. Both centrosomes were ablated, while t =0 s represents the ablation of the second and final centrosome. Dependent on the time-point of ablation, the posterior PAR domain formed (upper row) or failed to form (lower row). Scale bar, 5 µm. **d** The PAR-2 domain at the moment of the final centrosome ablation. Green line: theoretically predicted transition state. Yellow: zygotes that formed a posterior PAR domain after centrosome ablation (N=7); grey: zygotes that did not form a domain (N=5). Insert: Integrated number of cortical PAR-2 for all zygotes from panel d. Yellow, right column: posterior PAR domain formed (N=7), grey, left column: posterior PAR domain failed to form (N=5), green: transition state.

DATA AND CODE AVAILABILITY STATEMENT

All data generated or analyzed in this study, as well as code to analyze data and perform numeric simulations is available upon request.

METHODS

C. elegans strains and growth conditions

All strains were maintained at 18 °C and imaged at room temperature. Prior to imaging, *C. elegans* was transferred to 24 °C for 12-16 h. To obtain embryos, adult worms were dissected in M9 buffer (22 mM KH_2PO_4, 42 mM Na_2HPO_4, 86 mM NaCl) and mounted on agarose pads for imaging. All *C. elegans* strains, used in this study, are described in Supplementary Table 4. RNA interference was performed using the feeding method, as described in [46]. Feeding times were standardized for each condition, and were typically between 16 h to 24 h.

Image acquisition

All spinning-disk confocal movies of *C. elegans* zygotes were, except otherwise noted, acquired at room temperature, using a Zeiss axiovert observer Z1 equipped with a CSU-X1 Yokogawa spinning disk head using a 63X / 1.2 NA PlanApochromat objective and a Andor iXon emCCD camera. Measurements of the threshold velocity for polarity establishment were performed using the same system equipped with a Hamamatsu ORCA-Flash4.0 V2 CMOS camera. Concentration measurements were performed by acquiring one confocal stack in the mid-plane of the *C. elegans* zygote with a frame rate of 10 seconds, to reduce photobleaching to below 5 % for 500 seconds. Given a typical number of frames per movie of about 70, we estimate the effect of photobleaching to about 5 % over the course of our experiments (Supplementary Fig. 3d). NMY-2 GFP movies used for flow measurements were obtained in the mid-plane with a frame rate of 1 second, while NMY-2 mKate movies were captured with a frame rate of 2 seconds. Fluorescent Correlation Spectroscopy measurements were acquired with a Zeiss LSM 780 confocal microscope.

FRAP on NMY-2

We performed the Fluorescence Recovery After Photobleacing experiments using an Andor FRAPPA system. We acquired the images as cortical Z-stacks of three planes at 0.5 µm spacing with an interval time of 2 sec between individual stacks (iQ software, Andor Technology). We performed FRAP on GFP-labeled NMY-2 by bleaching a square of (9 µm X 9 µm) with a laser dwell time of 20 µs per pixel. We monitored the recovery for a subsquare (6 µm X 6 µm) at the center of the bleach square. We fitted the recovery curves of each FRAP experiment and determined the characteristic recovery time by fitting the fluorescence-intensity data with an exponential function, from which the mean as well as the standard error of the mean was calculated (Supplementary Fig. 2d-g). In case that the protein reached a steady-state concentration before the FRAP event, this recovery time scale is identical to the dissociation time scale of the bleached protein (Supplementary Discussion 1.2, Supplementary Fig. 1).

Membrane-associated concentration evaluation (MACE)

The fluorescence intensity for GFP, mCherry and mKate2 was calibrated as follows. Initially, we determined the concentration of an *in vitro* stock solution of GFP, mCherry and mKate2, using a Varian Cary 4000 UV-Vis Spectrophotometer. We then measured the fluorescence intensity of these solutions with known fluorophore concentration, for six concentration values, ranging typically from 500 nM to 10 µM. For each concentration value, we recorded between six to twelve individual intensity measurements, always using a freshly prepared sample. After correcting for camera flatness, we determined the average fluorescence for each measurement as well as the standard deviation between measurements for the same concentration. The corresponding calibration curves are shown in Supplementary Fig. 3e. The calibration factor w was extracted using linear fitting. For a homogeneous fluorophore concentration, the confocal intensity readout per pixel is given by: $I = i \cdot N$, with i as the intensity per fluorophore and N the number of fluorophores in the confocal volume. This leads to: $I = iV\rho_{solution} = w \cdot \rho_{solution}$, with V the confocal volume and $\rho_{solution}$ the fluorescence volume density. We obtained w= 21.7 $\pm$ 2.2 counts$\cdot$ µm^3 for eGFP, w= 10.7 $\pm$ 2.0 counts$\cdot$ µm^3 for mCherry, w= 14.6 $\pm$ 1.4 counts$\cdot$ µm^3 for mNeonGreen, and w= 22.5 $\pm$ 3.6 counts$\cdot$ µm^3 for mKate2. Errors are the 95% confidence interval of a linear regression.

Measuring cytoplasmic concentration over time

The cytoplasmic concentration of PAR-2 (or PAR-2 MT-) and PAR-6 was measured as follows. Initially, for each movie, we subtracted the background intensity and the autofluorescence of N2 *C. elegans* zygotes. The average fluorescence intensity per pixel of the cytoplasm was determined by averaging between the mean fluorescence intensity of three 4.34 X 4.34 μm ROI's inside the zygote. The average fluorescence intensity was converted to concentration using the measured conversion factor w, as explained above (see also [25]).

Determining the point-spread function

Quantifying the fluorescence intensity, originating from the membrane-bound protein fraction, requires the characterization of the broadening of the emitted fluorescent light due to diffraction and scattering inside the *C. elegans* zygote. Therefore, we measured the point-spread function of GFP and mCherry tagged PH-domain as membrane-bound reporter. In Supplementary Fig. 3g,h, we show the fluorescence intensity of PH::GFP and PH::mCherry in the maintenance phase. The intensity profile, perpendicular to the membrane was extracted around the cell-periphery, using image segmentation via the Matlab KoreTechs package [47]. For each intensity profile along the membrane, we fitted a Gaussian function added to an error function, which accounts for the higher cytoplasmic concentration, compared to the cell exterior,

$$I(x) = C + \frac{I_g}{\sigma_g\sqrt{2\pi}} e^{-\frac{(x-x_0)^2}{2\sigma_g^2}} + I_{cyto}/2 \cdot (\mathrm{erf}(x-x_0)+1)$$

with C as the background, I_g and σ_g as the amplitude and width of the Gaussian, I_{cyto} the intensity of the cytoplasm and x_0 as the position of the membrane. We fitted each individual profile along the membrane (typically around 300 profiles per frame) and determined the average width per embryo, which we repeated for several embryos. This yielded $\sigma_g = 329.6$ nm $\pm$ 7.3 nm (STD) (PH::GFP, N=8) and $\sigma_g = 320.7$ nm $\pm$ 18.9 nm (STD) (PH::mCherry, N=9). We compared this width to the width of the point spread function of individual 100 nm TetraSpeck fluorescence beads (Invitrogen) to σ = 185 nm in x and y and 510 nm in z (N=6) (Supplementary Fig. 3k). We assume that the dominating factor of the broadening of the membrane-associated signal originates from light scattering inside the *C. elegans* zygote, which explains the slightly larger width of the diffraction signal for light with shorter wavelength.

Measuring kymographs of protein concentration at the membrane

In short, spatiotemporal concentration measurements were performed in two steps. First, kymographs for NMY-2, PAR-2 and PAR-6 were determined, using custom-developed MATLAB code (see also [48]), which, similar to deconvolution, recovers the integrated, diffraction-corrected fluorescence intensity coming from fluorescently tagged proteins, which in our case are membrane-associated. Second, we used this fluorescence intensity to infer protein concentrations using a calibration procedure similar to [25]. In detail, all movies were background- and autofluorescence subtracted. Then, each frame of individual movies was segmented, using the KoreTechs Package [47]. Each segmentation was converted in a Bezier-smoothed curve with a separation of one pixel size between adjacent segmentation points. For all frames and all segmentation points, the fluorescence intensity profile perpendicular to the cell membrane was determined, for a length of 4.3 µm. The fluorescence signal of membrane-bound proteins is broadened due to diffraction, with a point spread function

$$PSF = \frac{1}{\sigma_x \sigma_y \sigma_z (2\pi)^{3/2}} e^{-(\frac{x^2}{2\sigma_x^2}+\frac{y^2}{2\sigma_y^2}+\frac{z^2}{2\sigma_z^2})}.$$

Since σ characterizes the length where the amplitude drops by $e^{-0.5}$, the PSF volume is characterized by

$$\frac{x^2}{\sigma_x^2}+\frac{y^2}{\sigma_y^2}+\frac{z^2}{\sigma_z^2}=1,$$

with a volume of

$$V_{PSF} = \frac{4}{3}\pi\sigma_x\sigma_y\sigma_z$$

and an illuminated area of a membrane in the x-z plane

$$A_{PSF} = \pi \sigma_x \sigma_z.$$

This implies that the surface concentration is given by:

$$\begin{aligned}\sigma &= \frac{N}{A_{PSF}} = \frac{\langle \rho \rangle V_{PSF}}{A_{PSF}} = \frac{I V_{PSF}}{w A_{PSF}} \\ &= \frac{4}{3} \sigma_y I w^{-1}.\end{aligned}$$

Here, σ denotes the surface concentration, N the number of proteins in the confocal volume, A_{PSF} the surface of the membrane, illuminated by the confocal microscope, V_{PSF} the volume of the point-spread function, σ_y the width of the point-spread function in the y-direction, ρ the fluorophore density, w the fluorescence calibration factor (Supplementary Fig. 3e) and I the intensity. Note that we choose the coordinate system such that x and z lie in the membrane plane and y is perpendicular to the membrane. The fluorescence intensity I was obtained by, for each individual profile along the membrane, fitting the intensity profile with:

$$I(x) = \frac{I}{\sigma_y \sqrt{2\pi}} e^{-\frac{(x-x_0)^2}{2\sigma_y^2}} + I_{cyto}/2 \cdot (\mathrm{erf}(\sigma_y^{-1}(x - x_0)) + 1)$$

We binned these resulting kymographs over 2.17 μm in space (10 pixel).

Generating ensemble-averaged concentration and flow fields

We synchronized individual kymographs in space and time using the geometric posterior pole and the beginning of cortical flows as reference points ($x = 0$, $t = 0$). For PAR concentration fields for *mlc-4* RNAi, we synchronized individual kymographs in time to the onset of cytokinesis. We then characterized the time between polarity establishment and cytokinesis to typically 850 s, and then generated ensemble averaged PAR concentration fields where $t = 0$ denotes triggering of polarity establishment. For creating an ensemble averaged concentration field, we discarded all measurements that show non-stereotypic initiation of cortical flows, away from the posterior pole

(with a tolerance of 10 μm).

Determining total protein amounts

We determine the total protein amount as the sum of the cortical and the cytoplasmic amount. The cytoplasmic amount was determined by determining the average cytoplasmic concentration, as explained above, and integration over the ellipsoidal zygote, using a=27 μm, b=15 μm and c=15 μm as semi-axis of the ellipsoid. The cortical amount was determined by first generating calibrated kymographs of the protein of interest. We then integrated the protein amount over the ellipsoid. Therefore we first reparameterized the kymographs from distance to the posterior to angle with respect to the anterior-posterior axis. Simplifying the embryonic shape as ellipsoid, we can then integrate the protein amount using:

$$P_{\text{total}}(t) = \int_0^{2\pi}\int_0^{\pi} \sqrt{b^2c^2\sin^4(\phi)\cos^2(\Theta) + a^2c^2\sin^4(\phi)\sin^2(\Theta) + a^2b^2\sin^2(\phi)\cos^2(\Theta)} \cdot P(\phi,\Theta)d\phi d\Theta$$

with $P_{\text{total}}(t)$ the protein amount on the cell surface and $P(\phi,\Theta)$ as the protein concentation on the cell surface. Assuming azimuthal symmetry, a kymograph along Θ provides sufficient information on the total cortical bound protein fraction (Supplementary Fig. 3i,j,l-q).

FCS measurement of the total protein amounts

We first determined the confocal volume of the Zeiss LSM 780 confocal microscope. Therefore we measured autocorrelation spectra for GFP in solution, with 4 different concentrations (300 nM, 100 nM, 10 nM, 3 nM). Fitting each autocorrelation allows for the determination of the number of fluorophores in confocal volume, which translates to a confocal volume in the case that the fluorophore concentration is known [49], yielding $V_{\text{conf}} = 3.2994e^{-16}l$. Next we determined the number of PAR-2::GFP molecules inside the confocal volume, in the one-cell *C. elegans* embryo by measuring autocorrelation spectra, for six embryos at a total of 21 different locations. We calculated the concentration, measured by FCS by dividing the number of PAR-2::GFP by the confocal volume (Supplementary Fig. 3a-c).

Determining the NMY-2 association rate

The association rate of NMY-2 from the cytoplasm to the actin cortex was calculated, assuming local binding equilibrium (Supplementary Figure 2a,c), such that $M = \frac{k_{\text{on},M,\text{eff}}}{k_{\text{off},M,\text{eff}}}$, with M the cortical NMY-2 concentration, $k_{\text{on},M,\text{eff}}$ the effective association rate and $k_{\text{off},M,\text{eff}}$ the effective dissociation rate. Using FRAP, we measured $k_{\text{off},M,\text{eff}}$ (Fig. 1b), while using MACE, we measured M (Supplementary Fig. 2a,b) in the anterior and the posterior domain. We thus calculated the effective association rate in both domains to: posterior: $k_{\text{on},M,\text{eff},P} = 2.1 \pm 0.4\,\mu\text{m}^{-2}\text{s}^{-1}$, anterior: $k_{\text{on},M,\text{eff},A} = 1.9 \pm 0.4\,\mu\text{m}^{-2}\text{s}^{-1}$. Thus, the effective association rate appears identical, in both domains, with an average of $k_{\text{on},M,\text{eff}} = 2.0 \pm 0.4\,\mu\text{m}^{-2}\text{s}^{-1}$. The effective association rate and the association rate of NMY-2 ($k_{\text{on},M}$) are related via $k_{\text{on},M,\text{eff}} = k_{\text{on},M} M_{\text{Cyto}}$, with M_{Cyto} the cytoplasmic NMY-2 concentration. We measured the average NMY-2 cytoplasmic concentration for the wild type to $M_{\text{Cyto}} = 10.4 \pm 1.4\,\mu\text{m}^{-3}$ (Supplementary Fig. 3m). We therefore obtained the NMY-2 association rate $k_{\text{on},M} = 0.199 \pm 0.04\,\mu\text{ms}^{-1}$.

Determining the ratio of labeled to unlabeled protein

For our quantification of the PAR-2 and PAR-6 amount, we used strains that posses a fluorescently tagged transgene and the endogenous, untagged gene. We quantified the ratio of labeled to unlabeled protein by western blotting *C. elegans* embryos against PAR-2 and PAR-6 (Supplementary Fig. 3f). We found a ratio of GFP labeled to unlabeled PAR-2 of 0.91 and a ratio of mCherry labeled to unlabeled PAR-6 to 0.71.

Determining the width of the posterior domain

The posterior PAR domain width was determined at each time point, by fitting the function $P_1\left[\text{erf}\left((x-P_2)/P_4\right) - \text{erf}\left((x-P_3)/P_4\right)\right] + P_5$, to the ensemble-averaged concentration of PAR-2 as well as the theoretical prediction of the PAR-2 concentration. The domain width was then given by $P_3 - P_2$. The experimental error was obtained by also fitting the above function to each individual movie of polarity establishment of the ensemble (N=6, unperturbed, N=9, PAR-2 MT-) and calculating the standard error of the mean of the quantity $P_3 - P_2$. For very small domains, this fitting routine becomes sensitive to the experimental noise profile. We thus restrained domain fitting of the experimental profiles to time-points where the fitting procedure detected a finite

domain in the theoretical prediction.

NMY-2 diffusion constant bound to the actomyosin cortex

We measured the diffusion constant of GFP-labeled NMY-2 mini-filaments by analyzing individual mini-filament trajectories. We imaged *C. elegans* zygotes with a frame rate of 5 Hz and analyzed these movies using u-track [50]. During the flow-phase, we found that the mean square displacement grows quadratic in time, as expected for directed movement (Supplementary Fig. 4a). We inhibited cortical flows and thus the directed motion of NMY-2 using *ect-2* RNAi. Then the mean square displacement grew linear in time, indicating diffusive motion (Supplementary Fig. 4b,c). We analyzed 7 movies of GFP-tagged NMY-2 under the *ect-2* RNAi condition. We restricted our analysis to NMY-2 tracks with a minimum length of 3 seconds, resulting in 657 tracks in total. Fitting the mean square displacement with a linear function yields $D_M = (0.054 \pm 0.08)\,\mu m^2 s^{-1}$. Here the uncertainty was evaluated by quantifying the standard deviation of the diffusion constant among the 657 tracks.

Trajectory analysis of the PAR-myosin system

We represent the temporal evolution of the PAR - actomyosin patterning system by the trajectory of the total number of cortical or membrane-bound PAR-2, PAR-6 and NMY-2, which change in time according to equations 1-6. Practically, we integrated the theoretical prediction for the unperturbed PAR-myosin system over the entire cortex (Fig. 3k,l). We observe that the membrane-bound PAR-6 numbers reduce marginally, that NMY-2 numbers decrease for an interval of about 350 seconds and that the PAR-2 numbers increase in time – a characteristic of the formation of the posterior PAR domain (Fig. 4a). We investigated the transition point of this pattern forming system, which characterizes the following: Initially the system is in a stable, homogeneous state and the cues drive the system towards the patterned state. If the cues are all inactivated shortly after their activation, the self-organized interactions carry the PAR - actomyosin system back to the homogeneous state. If the cues are however active for a longer time, the system can cross the transition point, from which point on the self-organized interactions will carry the system to the patterned state, even when the cues are inactivated (Supplementary Fig. 8a).

Separating guidance from self-organized components during trajectory analysis

In Supplementary Equations (33-35), we separated interactions that give rise to PAR polarity establishment into self-organized (Supplementary Equations (22-24)) and guidance interactions (Supplementary Equations (25,26)). These interactions give rise, at each time-point, to a change in the number of cortical PAR-2, PAR-6 and NMY-2. In Fig. 4a, we display the projection of the guidance-dynamics and the self-organized dynamics on the trajectory of the PAR - actomyosin system. Notably, we observed that initially the cues drive the system from the unpolarized system to the domain state, while the self-organized dynamics aims to drive the system back to the unpolarized state. This situation changes at around $t = 260\ s$. From then on, the self-organized dynamics dominates over the guidance dynamics and drives the zygote to the polarized state.

Determining the critical flow velocity for polarization via flows

To measure the threshold velocity for polarity establishment, we monitored the fluorescently tagged PAR-2 and PAR-6 (using the SWG025 strain) in the confocal mid-plane of the zygote. These embryos were exposed to a range of different feeding times of *mlc-4* RNAi. We determined cortical flow velocities for *mlc-4* RNAi by investigating the displacement-field of yolk granules adjacent to the actomyosin cortex, using the freely available PIVlab MATLAB algorithm [51]. 2D velocity fields were obtained as in [20] (Supplementary Fig. 7c). Each embryo then was classified as polarized or unpolarized by monitoring the occurrence of a posterior PAR domain close to cytokinesis and an asymmetric cell division. We determined the theoretical prediction by calculating the spatiotemporal solutions of the PAR - actomyosin system for different values of the scaled contractility strength C_*/γ. For each solution, we monitored the peak actomyosin flow velocity and the maximum PAR-2 concentration 500 seconds after polarity triggering. We determined the critical flow velocity by fitting the data to $C_{P2}(v) = A \cdot \tanh(B \cdot (v - v_{crit})) + 1) + C$, with A the saturation value, B the steepness, C the offset and v_{crit} the critical flow velocity.

Determining the transition-state PAR-2 domain size by centrosome laser ablation

Laser ablation of the centrosome was performed in a C. elegans strain with SPD-2 labeled with GFP and PAR-2 labeled with mNeonGreen, while using *mlc-4* RNAi. We conducted centrosome ablation using methods similar to those in [20].We performed ablation by applying 10 ultraviolet

pulses at 1 kHz on the circumference of a circle with a diameter of 0.5 μm at 9 equidistant sites. We ablated both centrosomes at different time-points during the first cell stage, when their distance to the membrane was larger than typically 2 μm, to avoid membrane rupture. After ablation, we imaged the zygote for typically 5 minutes. We scanned for the re-appearance of the centrosome, which occurs in case the centrosome was only bleached, for cell rupture or for membrane damage, resulting in cytoplasmic leakage, and excluded all these from our data-set. From 72 centrosome ablation experiments, 12 were considered successful. At the time-point of the second centrosome ablation, we used MACE to measure the spatial profile of the PAR-2 domain as well as the integrated number of cortical PAR-2.

ACKNOWLEDGMENTS:

P.G. acknowledges a EMBO Long-Term Fellowship for funding. K.V.K.'s research is supported by the Department of Biotechnology, India through a Ramalingaswami re-entry fellowship, and the Max Planck Society and the Department of Science and Technology, India through a Max Planck Partner Group at ICTS-TIFR. N.W.G. was supported by the Francis Crick Institute, which receives its core funding from Cancer Research UK (FC001086), the UK Medical Research Council (FC001086), and the Wellcome Trust (FC001086) and is a member of the GENiE network supported by COST Action BM1408 and EMBO. S.W.G was supported by the DFG (SPP 1782, GSC 97, GR 3271/2, GR 3271/3, GR 3271/4), the European Research Council (grant No 281903 and 742712), ITN grants 281903 and 641639 from the EU, the Max-Planck-Society as a Max-Planck-Fellow, and the Human Frontier Science Program (RGP0023/2014). J.S.B. acknowledges the Human Frontier Science Program for funding. We thank Dan Dickinson, Bob Goldstein, Fumio Motegi, and Geraldine Seydoux for sharing *C. elegans* strains. We thank Pierre Gönczy, Lars Hubatsch, Tony Hyman, Karsten Kruse, and Michel Labouesse for discussion and insightful comments on the manuscript.

AUTHORS CONTRIBUTION:

P.G. performed experiments and K.V.K. developed the theory, with help from all authors. Data was analyzed together with input from all authors, and P.G., K.V.K., F.J. and S.W.G. wrote the manuscript.

COMPETING INTERESTS:

The authors declare no competing interests.

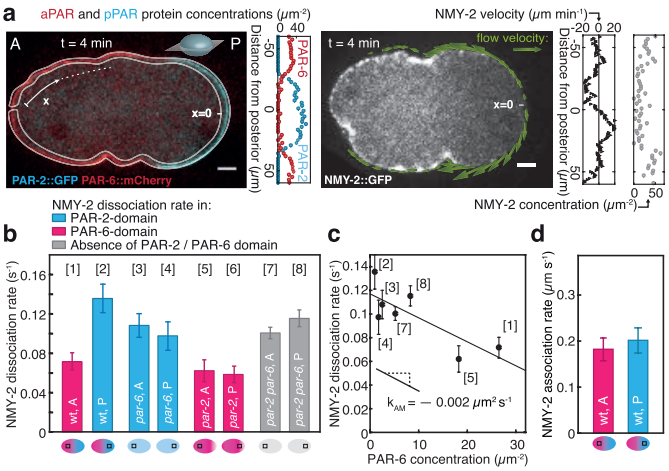
a
aPAR and pPAR protein concentrations (μm⁻²)
NMY-2 velocity (μm min⁻¹)
A
t = 4 min
P
x
x=0
PAR-2::GFP PAR-6::mCherry
PAR-6
PAR-2
Distance from posterior (μm)
t = 4 min
flow velocity:
x=0
NMY-2::GFP
NMY-2 concentration (μm⁻²)
b
NMY-2 dissociation rate in:
PAR-2-domain
PAR-6-domain
Absence of PAR-2 / PAR-6 domain
NMY-2 dissociation rate (s⁻¹)
[1] [2] [3] [4] [5] [6] [7] [8]
wt, A
wt, P
par-6, A
par-6, P
par-2, A
par-2, P
par-2 par-6, A
par-2 par-6, P
c
NMY-2 dissociation rate (s⁻¹)
[2] [3] [8] [7] [4] [1] [5]
k_AM = — 0.002 μm² s⁻¹
PAR-6 concentration (μm⁻²)
d
NMY-2 association rate (μm s⁻¹)
wt, A
wt, P

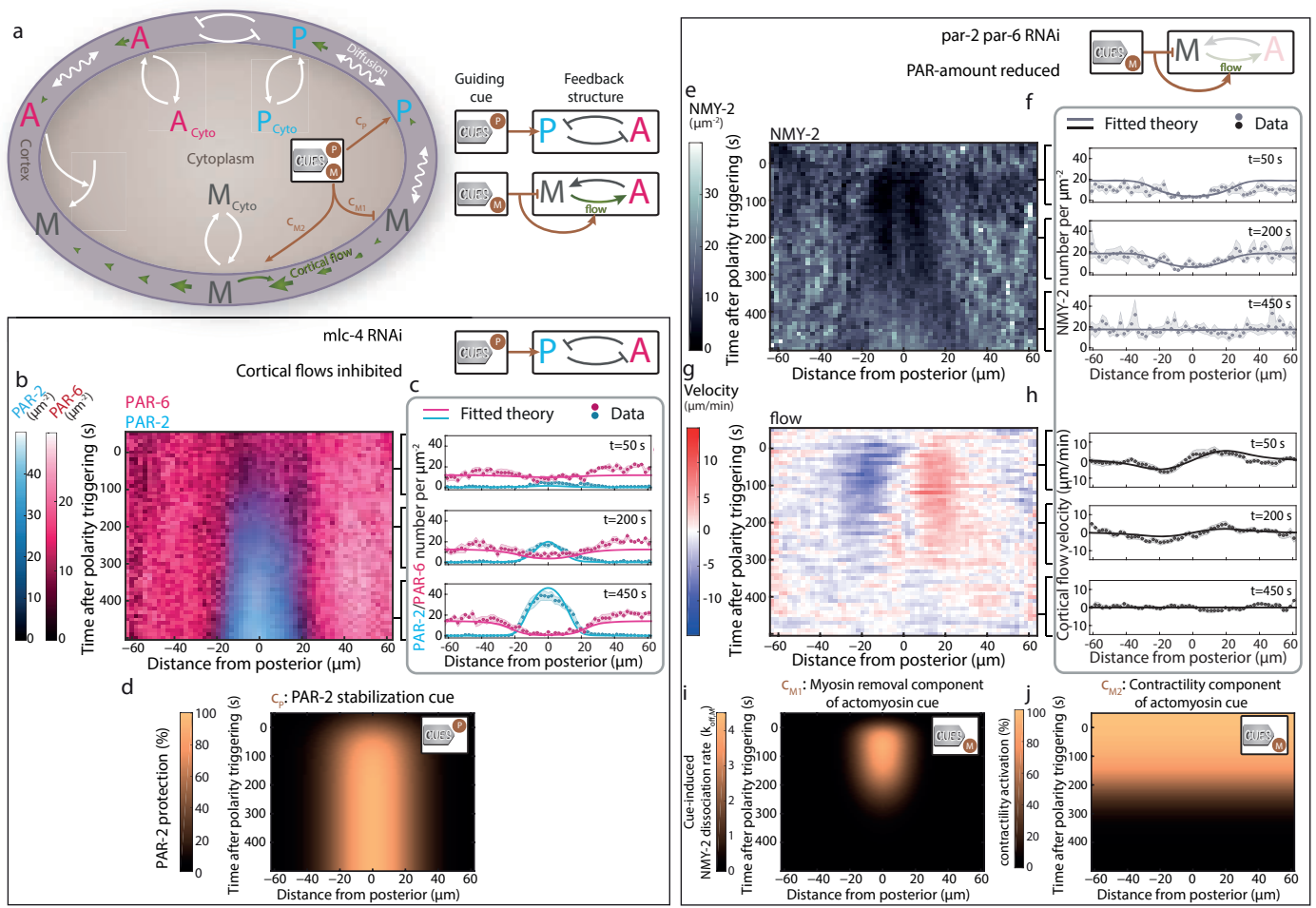
a
A
P
Diffusion
A Cyto
P Cyto
Cytoplasm
Cortex
M Cyto
M
Cortical flow
Guiding cue
Feedback structure
flow
mlc-4 RNAi
Cortical flows inhibited
b
PAR-2 (μm⁻²)
PAR-6 (μm⁻²)
PAR-6
PAR-2
Time after polarity triggering (s)
Distance from posterior (μm)
c
Fitted theory
Data
PAR-2/PAR-6 number per μm²
t=50 s
t=200 s
t=450 s
d
C_P: PAR-2 stabilization cue
PAR-2 protection (%)
par-2 par-6 RNAi
PAR-amount reduced
e
NMY-2 (μm⁻²)
NMY-2
f
NMY-2 number per μm²
g
Velocity (μm/min)
flow
h
Cortical flow velocity (μm/min)
i
C_{M1}: Myosin removal component of actomyosin cue
Cue-induced NMY-2 dissociation rate (k_{offM})
j
C_{M2}: Contractility component of actomyosin cue
contractility activation (%)

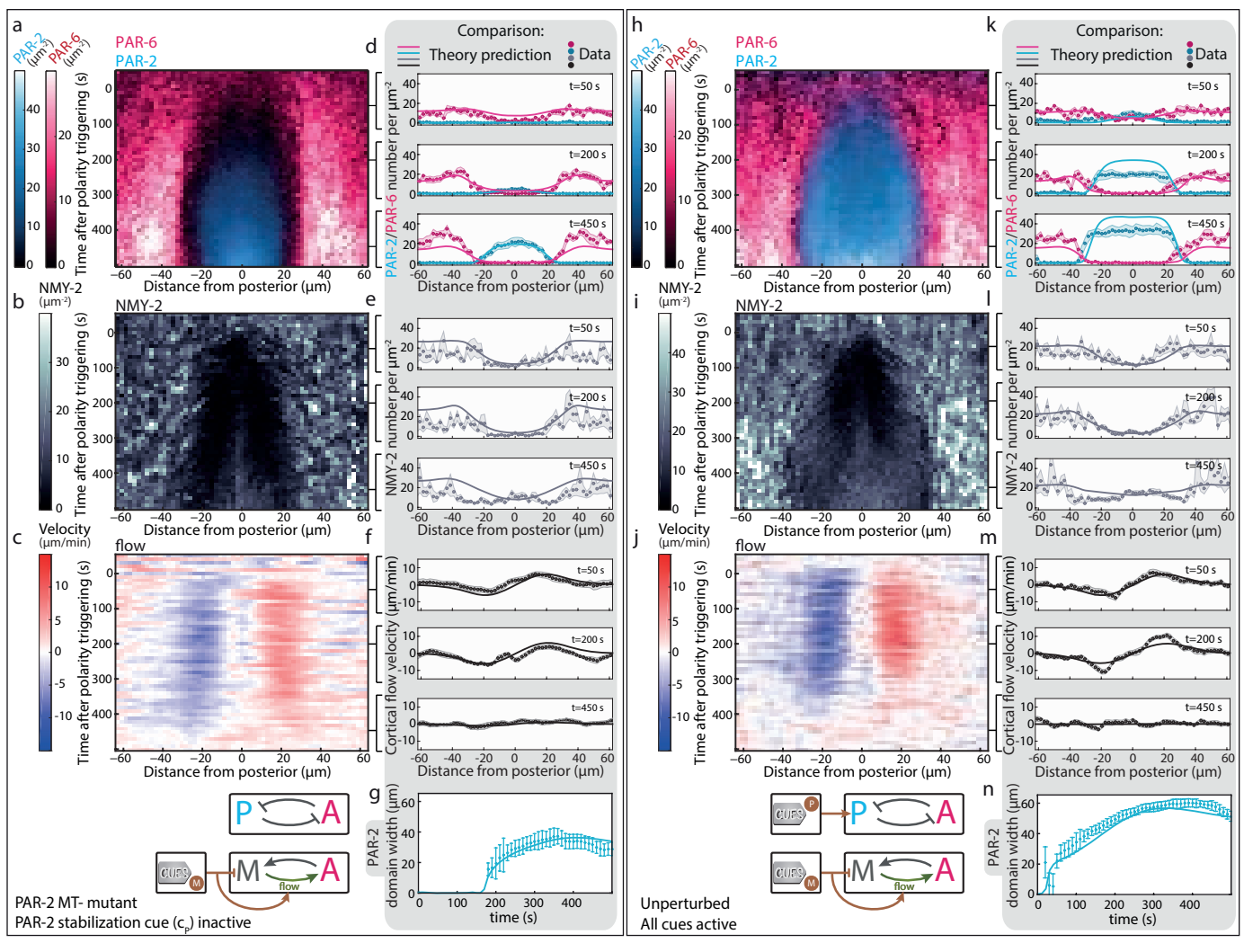
a
PAR-2 (μm⁻²)
PAR-6 (μm⁻²)
PAR-6
PAR-2
Time after polarity triggering (s)
Distance from posterior (μm)
b
NMY-2 (μm⁻²)
NMY-2
c
Velocity (μm/min)
flow
d
Comparison:
Theory prediction
Data
t=50 s
t=200 s
t=450 s
PAR-2/PAR-6 number per μm²
e
NMY-2 number per μm²
f
Cortical flow velocity (μm/min)
g
PAR-2 domain width (μm)
time (s)
P
A
M
CUF3
flow
PAR-2 MT- mutant
PAR-2 stabilization cue (c_p) inactive
h
i
j
k
l
m
n
Unperturbed
All cues active

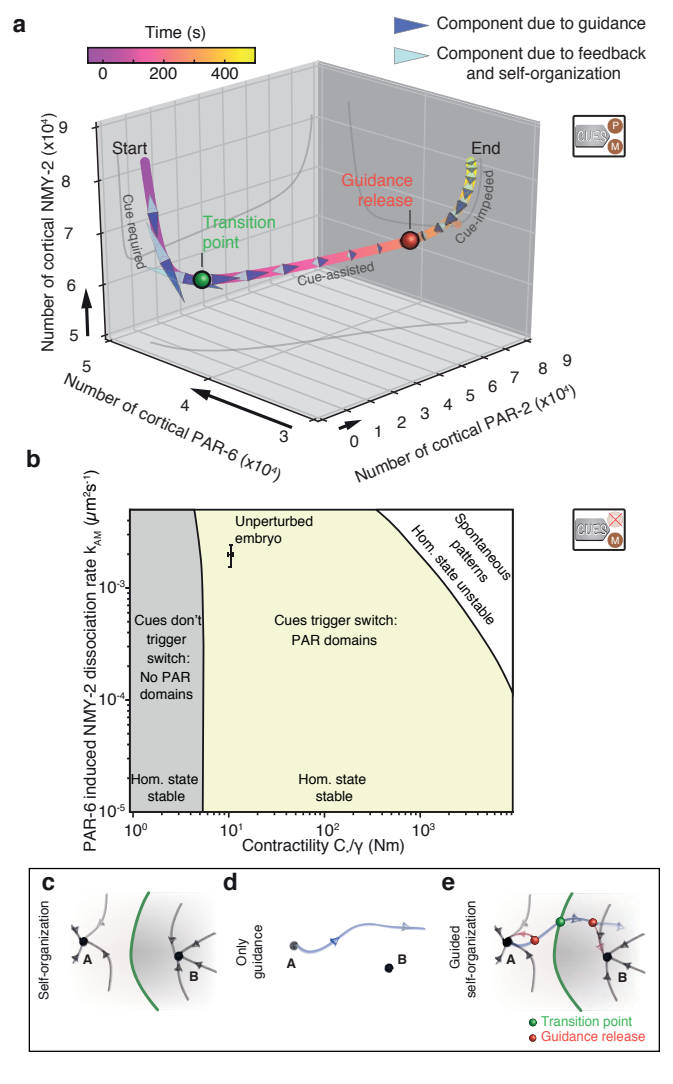
a
Time (s)
0
200
400
Component due to guidance
Component due to feedback and self-organization
Start
End
Guidance release
Transition point
Cue-required
Cue-assisted
Cue-impeded
Number of cortical NMY-2 (x10⁴)
Number of cortical PAR-6 (x10⁴)
Number of cortical PAR-2 (x10⁴)
b
Unperturbed embryo
Spontaneous patterns
Hom. state unstable
Cues don't trigger switch: No PAR domains
Cues trigger switch: PAR domains
Hom. state stable
Hom. state stable
PAR-6 induced NMY-2 dissociation rate k_AM (μm²s⁻¹)
Contractility C_c/γ (Nm)
c
Self-organization
A
B
d
Only guidance
A
B
e
Guided self-organization
A
B
Transition point
Guidance release

weaker-to-stronger cue titration

a

PAR-2 MT- PAR-6

V= 3.0 μm min^{-1} V= 4.3 μm min^{-1}

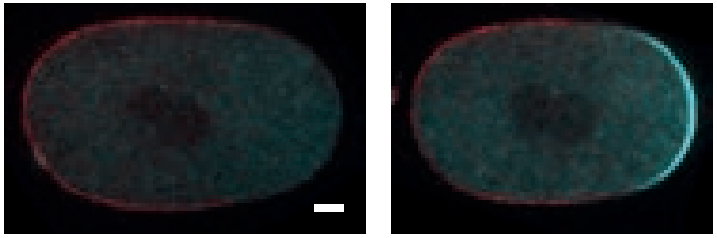

b

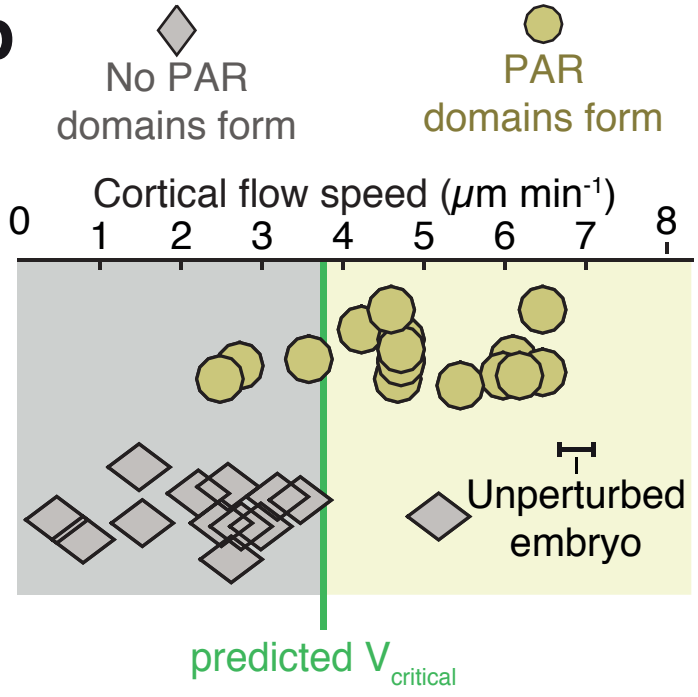

shorter-to-longer cue titration

c

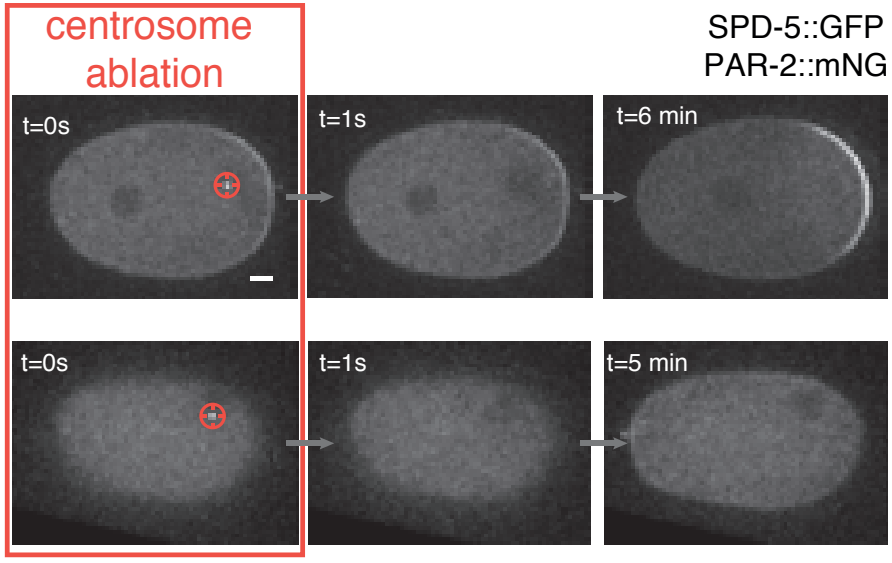

d

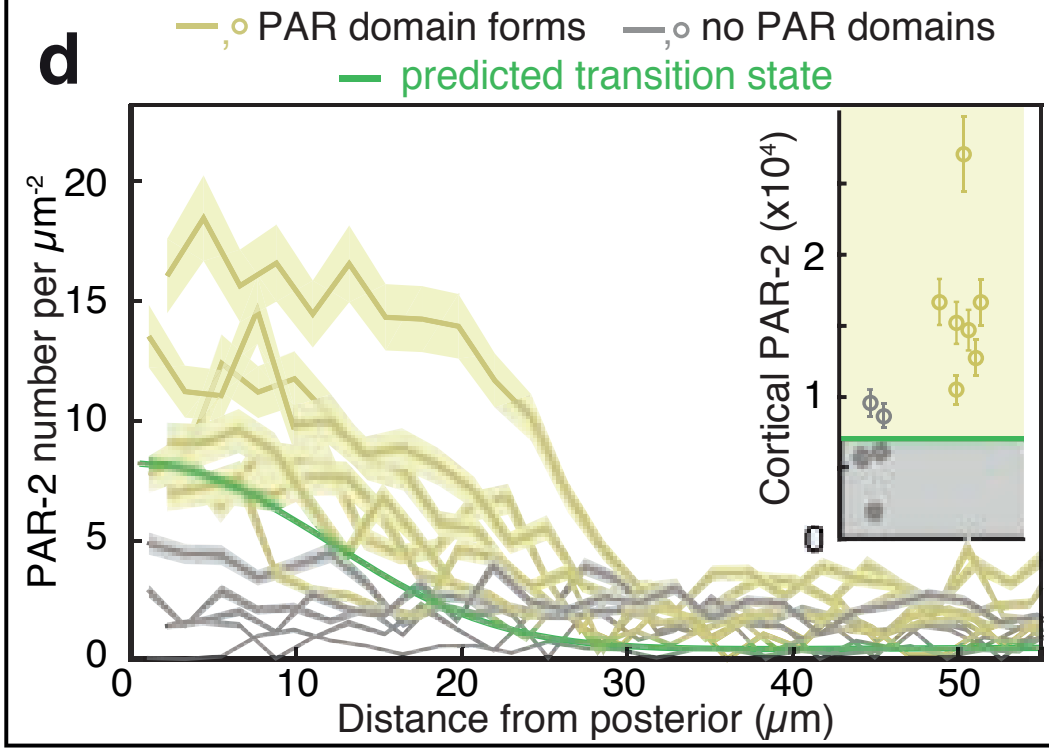

Supplementary Information for: Guiding self-organized pattern formation in cell polarity establishment

Peter Gross[1,2,3,†], K. Vijay Kumar[4,3†], Nathan Goehring[5,6], Justin S. Bois[7], Carsten Hoege[2], Frank Jülicher[3], Stephan W. Grill[1,2,3*]

Affiliations: [1]BIOTEC, TU Dresden, Tatzberg 47/49, 01307, Dresden, Germany

[2]Max Planck Institute of Molecular Cell Biology and Genetics, Pfotenhauerstrasse 108, 01307 Dresden, Germany

[3]Max Planck Institute for the Physics of Complex Systems, Nöthnitzer Strasse 38, 01187 Dresden, Germany

[4]International Centre for Theoretical Sciences, Tata Institute of Fundamental Research, Bengaluru 560089, India

[5]The Francis Crick Institute, 1 Midland Road, London NW1 1AT, UK

[6]Medical Research Council Laboratory for Molecular Cell Biology, Gower Street, University College London, London WC1E 6BT, UK

[7]California Institute of Technology, 1200 E California Blvd, Pasadena, CA 91125, USA

[†]These authors contributed equally [*]To whom correspondence should be addressed; E-mail: stephan.grill@biotec.tu-dresden.de.

1 Supplementary Discussion

1.1 The effect of PAR proteins on NMY-2 is negligible during *par-2* and *par-6* double RNAi

We investigated the effect of the PAR proteins on NMY-2 concentrations during *par-2* and *par-6* double RNAi as follows. First we determined the reduction of PAR-2 and PAR-6 amounts, during *par-2* and *par-6* double RNAi and *par-6* RNAi (Supplementary Fig. 3n-q). We found that for *par-2* and *par-6* double RNAi, the total number of both proteins reduces down to approximately 30%, compared to the unperturbed condition. The decrease in PAR-6, part of the anterior PAR complex, which is the dominant NMY-2 regulator (Supplementary Fig. 2k), is more pronounced for *par-6* RNAi only (Supplementary Fig. 3n,p). We then compared the four parameters, obtained by fitting the NMY-2 concentration and flow profile, between the *par-2* and *par-6* double RNAi and the *par-6* RNAi condition. We observed that the four parameters changed only moderately, between both conditions (between 5% - 30%), (Supplementary Fig. 10). We furthermore compared the fit of the *par-2* and *par-6* double RNAi condition to a fit where we explicitly consider the experimentally measured surface concentration of PAR-2 and PAR-6, during *par-2* and *par-6* double RNAi. We fit the NMY-2 concentration profile and flow field, while explicitly considering how the PAR-6 concentration changes NMY-2 profiles, via the coupling constant k_{AM}. We observed that the four parameters changed between both conditions between 1% - 20% (Supplementary Fig. 11). We thus conclude that during *par-2* and *par-6* double RNAi, the PAR concentration fields can be neglected when describing the concentration fields of NMY-2 and its flow field.

1.2 The FRAP recovery time scale is identical to the NMY-2 dissociation rate

During the initial cortical flow phase, myosin locally exhibits pulsatory dynamics, with dynamic foci, structures of very high myosin concentrations (*1, 2*). This spatial and temporal inhomogeneity precludes a direct measurement of the NMY-2 dissociation rate with FRAP. We thus measure this quantity during the maintenance phase (t = 400s - 600s after polarity triggering), where myosin concentration is close to a steady state (Supplementary Fig. 2a,c), and extrapolate the measured dissociation rate to the cortical flow phase. The obtained spontaneous myosin dissociation rate is in good agreement with COMBI (co-moving mass balance imaging) measurements of myosin kinet-

ics in the flow phase (*2*), indicating that the binding kinetics of myosin do not change substantially during the early stage of the cell cycle.

1.2.1 Dynamical equations of the FRAP system

Consider a system of a membrane and a large cytoplasm. The concentration on the membrane is homogeneous and in a binding-unbinding equilibrium. The FRAP event happens in region S_2, while the region S_1 is not bleached. Also assume that the diffusivity of the molecule is small such that diffusive fluxes between the bleached and unbleached region can be neglected. This is actually the case for NMY-2, with its very low diffusion rate (Supplementary Table 2). In addition, we only analyze the central region of 6 X 6 μm of the bleached square of 9 X 9 μm to ensure that diffusion indeed does not matter for these experiments.
The fluorescent membrane concentration evolves by:

$$\partial_t c_1(t) = k_{on} c_{cyto}(t) - k_{off} c_1(t), \tag{1}$$

$$\partial_t c_2(t) = k_{on} c_{cyto}(t) - k_{off} c_2(t), \tag{2}$$

with $c_{cyto}(t)$, $c_1(t)$, and $c_2(t)$ the concentration of fluorescent particles in the cytoplasm, in region 1 and region 2 (the bleached region), respectively (see Supplementary Fig. 1a). k_{on} and k_{off} represent the equilibrium association and dissociation rates, respectively. The total number of particles is conserved:

$$N_{total} = const = N_{cyto} + N_1 + N_2, \tag{3}$$

with

$$N_{total} = V \cdot c_{cyto}(t) + S_1 \cdot c_1(t) + S_2 \cdot c_2(t), \tag{4}$$

such that (we use $\gamma = S_2/S_{tot}$ and $1-\gamma = S_1/S_{tot}$).

$$c_{cyto}(t) = \frac{N_{total}}{V} - \frac{S_1}{V} c_1(t) - \frac{S_2}{V} c_2(t) = \rho_{total} - \gamma\psi c_2(t) - (1-\gamma)\psi c_1(t); \tag{5}$$

Inserting this into eq. (1) and (2) results in:

$$\partial_t c_1(t) = k_{on}\rho_{total} - (1-\gamma)k_{on}\psi c_1(t) - \gamma k_{on}\psi c_2(t) - k_{off} c_1(t), \tag{6}$$

$$\partial_t c_2(t) = k_{on}\rho_{total} - (1-\gamma)k_{on}\psi c_1(t) - \gamma k_{on}\psi c_2(t) - k_{off} c_2(t), \tag{7}$$

This system of ordinary differential equations for c_1 and c_2 are thus coupled according to:

$$\partial_t \begin{pmatrix} c_1 \\ c_2 \end{pmatrix} = \begin{pmatrix} -k_{off} - (1-\gamma)k_{on}\psi & -\gamma k_{on}\psi \\ (\gamma-1)k_{on}\psi & -k_{off} - \gamma k_{on}\psi \end{pmatrix} \begin{pmatrix} c_1 \\ c_2 \end{pmatrix} + \begin{pmatrix} k_{on}\rho_{total} \\ k_{on}\rho_{total} \end{pmatrix} \tag{8}$$

With eigenvalues

$$\lambda_1 = -k_{off} - k_{on}\psi \tag{9}$$

$$\lambda_2 = -k_{off} \tag{10}$$

and the eigenvectors

$$e_1 = \begin{pmatrix} 1 \\ 1 \end{pmatrix} \tag{11}$$

$$e_2 = \begin{pmatrix} \frac{\gamma}{\gamma-1} \\ 1 \end{pmatrix} \tag{12}$$

1.2.2 Dynamics of the fluorescent population after the bleaching event

Let us only look at the fluorescent membrane concentration, after the FRAP event ($t = 0s$). For the initial condition, we assume that all molecules in the FRAP region are bleached and that outside of the FRAP region, the system is in binding-unbinding equilibrium. During the FRAP event, we bleach all molecules in region S_2. As initial conditions for the FRAP event, we assume that the concentration outside of the FRAP region is the equilibrium constant and inside the FRAP region it is zero:

$$c_1^o = \frac{k_{on}\rho_{total}}{k_{on}\psi + k_{off}}, \tag{13}$$

$$c_2^o = 0, \tag{14}$$

And the exact solution for this initial condition is:

$$\begin{pmatrix} c_1(t) \\ c_2(t) \end{pmatrix} = c_1^o \left[\gamma\left(\frac{\psi c_1^o}{\rho_{tot}} - 1\right) \begin{pmatrix} 1 \\ 1 \end{pmatrix} e^{-(k_{on}\psi + k_{off})t} + \begin{pmatrix} \gamma \\ \gamma - 1 \end{pmatrix} e^{-k_{off}t} + \left(1 - \gamma\frac{\psi}{\rho_{tot}}c_1^o\right) \begin{pmatrix} 1 \\ 1 \end{pmatrix} \right] \tag{15}$$

For small γ, the dynamics of the FRAP region ($c_2(t)$) is dominated by $e^{-k_{off}t}$, while the $e^{-(k_{on}\psi+k_{off})t}$ becomes increasingly important with increasing γ (Supplementary Fig. 1b,c). Numerical evaluations of the solution show that when the FRAP region is small compared to the total region, then the fluorescence recovery time-scale is in essence given by k_{off}. We use a FRAP region of 9 μm X 9 μm, which corresponds to a γ of about 0.02, and thus indeed in the region where k_{off} dominates the FRAP recovery time scale (Supplementary Fig. 1c).

2 Supplementary Equations

2.1 Model definition

We build a coarse-grained theory for the dynamics of the PAR-actomyosin system as follows. The sum total membrane-bound fraction, c, and the cytoplasmic fraction, c_{cyto}, of a protein c is a constant c_{tot}, throughout the polarity process (Supplementary Fig. 3i,j,l,m). Here c is either A, P or M. We write this constraint of limited protein pools as

$$c_{\text{tot}} = \oint_{\text{surface}} dS\, c + \int_{\text{cytoplasm}} dV\; c_{\text{cyto}}, \tag{16}$$

where dS and dV are surface and volume elements of the cell. For all the proteins involved (A,P,M), the cytoplasmic diffusion constants are much larger than their surface diffusion constants (*3*). As such, the cytoplasmic concentrations can be considered homogeneous. Within this approximation, the above equations for the number conservation take on the form

$$c_{\text{cyto}}(t) = \rho_c - \frac{1}{V}\oint_{\text{surface}} dS\, c(\mathbf{r},t) \tag{17}$$

where V is the total volume of the cell and $\rho_c = c_{\text{tot}}/V$, and $\mathbf{r}$ denotes a coordinate on the surface of the cell.

The spatiotemporal dynamics of the surface concentrations $c(\mathbf{r},t)$ are affected by three distinct physical processes: (i) surface transport by active hydrodynamic flows in the cortex, (ii) passive diffusive transport on the surface, and (iii) chemical reactions amongst the surface bound molecules and their cytoplasmic counterparts. As such, the transport equations take on the generic form

$$\partial_t c(\mathbf{r},t) = -\nabla\cdot(\mathbf{v}\,c) + D_c\nabla^2 c + R_c \tag{18}$$

where $\mathbf{v}(\mathbf{r},t)$ is the active hydrodynamic flow field in the actomyosin cortex, D_c is the diffusion constant, R_c represents the sum total of the reactions affecting c, and ∇ is a derivative operator on the cell surface. The hydrodynamics of the cortex is captured by a coarse-grained theory in which actomyosin activity generates active stresses in addition to the passive stresses (*4*). The total stress in a patch of the actomyosin cortex can be written as

$$\sigma_{\text{tot}} = \sigma_{\text{passive}} + \sigma_{\text{active}} \tag{19}$$

where σ_{passive} is the passive viscous stress arising in a hydrodynamic description of the cortex, and σ_{active} is the active stress arising from actomyosin activity. Neglecting inertia, the force-balance equation is

$$\nabla \cdot \sigma_{\text{tot}} = \gamma \mathbf{v} \tag{20}$$

where the term on the right-hand-side represents a simple frictional drag force on cortical flows due the surrounding cytoplasm/membrane (*4*). The active stress is up-regulated by the local concentration of NMY-2 like

$$\sigma_{\text{active}} = C_* \frac{M}{M + M_*}, \tag{21}$$

where C_* is the strength of contractility and M_* is a Hill coefficient. Any spatially inhomogeneous profile of myosin leads to an active stress, and gradients in this active stress generate flow (*4*).

2.2 Biochemical reactions

2.2.1 NMY-2 reactions

In addition to the turnover of the surface component of NMY-2 with the cytoplasmic component, the off-rate of NMY-2 was found to be regulated by the aPARs (Fig. 1c, main text). As such, the biochemical reactions that affect the surface NMY2 concentration can be written as

$$\tilde{R}_M = k_{\text{on},M} M_{\text{cyto}} - \left[k_{\text{off},M} - k_{AM} A\right] M \tag{22}$$

where $k_{\text{on},M}$ and $k_{\text{off},M}$ are the on- and off-rates to the cytoplasm, and k_{AM} is the coefficient of the regulation of the off-rate of NMY-2 by the anterior PARs. As evident from the above equation, the coupling k_{AM} cannot be arbitrarily large as this would make

the NMY-2 system unstable. However, as long as $\left[k_{\text{off},M} - k_{AM}\, A\right] > 0$, stability is ensured, a condition which was always met, in this study.

2.2.2 PAR reactions

The anterior and posterior PAR proteins have mutually antagonistic interaction between them (*5–9*). For the anterior PAR proteins, this antagonistic interaction occurs in the form of an on-rate regulation by the posterior PAR complex (*10, 11*), while for the posterior PAR complex, this realizes in the form of an off-rate regulation by the anterior PAR complex (*12*). Additionally, as discussed above, each PAR protein has a membrane-bound surface component and a cytoplasmic bulk component, with continuous exchange between these two components. Thus the biochemical interactions between the PAR proteins can be expressed as

$$R_A = \frac{k_{\text{on},A}}{(1 + k_{AP} P^{\alpha})} A_{\text{cyto}} - k_{\text{off},A}\, A \tag{23}$$

$$\tilde{R}_P = k_{\text{on},P}\, P_{\text{cyto}} - \left[k_{\text{off},P} + k_{PA}\, A^{\beta}\right] P \tag{24}$$

where $k_{\text{on},A}$ ($k_{\text{on},P}$) and $k_{\text{off},A}$ ($k_{\text{on},P}$) are the on- and off-rates of the anterior (posterior) PAR proteins, k_{AP} and k_{PA} are the coefficients of the mutually antagonistic interactions between them, and α, β are stoichiometric coefficients. This mutual antagonism between the PAR complexes leads to bistability in the possible states of the PAR system (*12–14*). Specifically, one finds that there are three main regions in the PAR parameters such that (i) only homogeneous PAR states are stable, (ii) only PAR domain states are stable, and (iii) stable states with homogeneous PAR profiles can coexist with PAR domain states that are also stable. In region (iii), a transition from the homogeneous state to the domain state require a non-uniform perturbation whose strength should exceed a certain magnitude in order to trigger transition into the domain state. This triggering of the self-organized state of the PAR system from the homogeneous state to the polarized domain state is guided by external cues arising from the centrosome.

2.3 Spatiotemporal cues that trigger the PAR system

The centrosome associated with the male pronucleus provides spatiotemporal cues that guide the PAR - actomyosin patterning process. The cues are spatially localized around the posterior pole, and act persistently for a finite period of time. Generally, the two guiding cues (PAR-2 stabilization cue, actomyosin cue) influence the PAR-actomyosin system via three interactions, with the actomyosin cue possessing two components:

1. PAR-2 stabilization cue: The microtubules associated with the centrosome lead to a reduction in the phosphorylation rate of PAR-2 (*15*). This ensures that the pPAR concentration locally rises, which in turn clears the aPARs and thus paves the way for the formation of a stable pPAR domain.

2. Myosin removal component of actomyosin cue: Through a yet undisclosed mechanism, the same centrosome locally depletes NMY-2 at the posterior pole (*16*) creating a spatial gradient in the cortical concentration NMY-2 (and hence the active stresses) which leads to cortical flows (Fig. 1a, main text). These flows clear out the anterior PARs, making way for the posterior PARs to nucleate a domain on the surface.

3. Contractility component of actomyosin cue: Additionally, NMY-2 contractility is up-regulated for a period of about 350s after triggering polarity establishment, by up-regulating RhoA, involving NOP-1 (*17*). By the end of the cortical flow period, cytoplasmic flows, which constrict the centrosome close to the actomyosin cortex at the posterior pole, also cease. Consequently, the timescale for which the centrosome remains in proximity to the actomyosin cortex and the timescale of actomyosin contractility is identical (Supplementary Fig. 5).

The above cues guide the PAR system to a proper polarized state starting from the homogeneous state. We note that the guiding-cue interactions (1) and (2), promoted by the centrosome (i) are localized in space near the posterior pole, (ii) gradually switch on when the centrosome approaches the posterior pole, and (iii) are 'on' for a finite time. With these considerations, we mathematically represent all three external cues by

$$\mathrm{c_P}(\mathbf{r},\mathrm{t}) = k_{PA} A^{\beta} P\, \kappa_P\, F_P(\mathbf{r})\, f_P(t), \tag{25}$$

$$\mathrm{c_{M1}}(\mathbf{r},\mathrm{t}) = -k_{\mathrm{off},M} M\, \kappa_M\, F_M(\mathbf{r})\, f_M(t), \tag{26}$$

$$\mathrm{c_{M2}}(\mathrm{t}) = f_C(t), \tag{27}$$

where κ_P and κ_M are the (dimensionless) strengths of the two cues. The functions $F_P(\mathbf{r})$ and $F_M(\mathbf{r})$ are localized near the posterior pole, and without loss of generality, we choose the a Gaussian functional form for their profiles

$$F_P(\mathbf{r}) = \exp\left(-\frac{(\mathbf{r}-\mathbf{r}_{\mathrm{posterior}})^2}{d_P^2}\right), \tag{28}$$

$$F_M(\mathbf{r}) = \exp\left(-\frac{(\mathbf{r}-\mathbf{r}_{\mathrm{posterior}})^2}{d_M^2}\right), \tag{29}$$

where $\mathbf{r}_{\text{posterior}}$ is the location of the posterior pole, d_P and d_M are the characteristic widths of the spatial profiles. Temporally, the PAR-2 stabilization cue and the myosin removal component of actomyosin cue switch on gradually from the off state, and persistently stay in the on-state for a finite time. The myosin removal cue component is active for a finite time and appears to switch off when the centrosome, attached to the male pronucleus detaches from the actomyosin cortex (Supplementary Fig. 5). Again, without loss of generality, we choose the following mathematical expression to describe temporal profile of the myosin removal cue component that switches on the trigger by transitioning from zero to one at $t = 0$ smoothly on the time scale $\tau_{M,\text{on}}$ and go back to zero after the time T_M, again smoothly on a time scale $\tau_{M,\text{off}}$:

$$f_M(t) = \frac{1}{2}\left[\tanh\left(\frac{t}{\tau_{M,\text{on}}}\right) - \tanh\left(\frac{t-T_M}{\tau_{M,\text{off}}}\right)\right]. \tag{30}$$

The PAR-2 stabilization cue is mediated by microtubules, emerging from the male pronucleus, which are in contact with the cortex even when the centrosome detaches from the cortex. Because of that, we describe the temporal profile of the PAR-2 stabilization cue by:

$$f_P(t) = \frac{1}{2}\left[\tanh\left(\frac{t}{\tau_{P,\text{on}}}\right) + 1\right], \tag{31}$$

which switches on the PAR-2 stabilization cue by transitioning from zero to one at $t = 0$ smoothly on the time scale $\tau_{P,\text{on}}$ and remaining on for the entire timescale of PAR polarity establishment. Since both the triggers arise from the same centrosome, the times at which the cues are turned 'on' are taken to be the same $t = 0$. The contractility cue component increases actomyosin contractility already before the centrosome provides the signal for polarity establishment, and decreases contractility at the same time that the centrosome leaves the proximity of the actomyosin cortex (Supplementary Fig. 5). We thus use the following temporal profile to describe the contractility cue:

$$f_C(t) = \frac{1}{2}\left[1 - \tanh\left(\frac{t-T_M}{\tau_{M,\text{off}}}\right)\right], \tag{32}$$

Note that the specific spatiotemporal profiles that we have chosen for the cues are generic. Other smooth forms are possible and would not lead to very different dynamics.

2.4 Complete model

With the considerations of the previous two sections, we can now write down the full set of biochemical reactions that govern the dynamics of A, P and M. They are

$$R_A = \frac{k_{\text{on},A}}{(1+k_{AP}P^{\alpha})} A_{\text{cyto}} - k_{\text{off},A}\, A, \tag{33}$$

$$R_P = k_{\text{on},P} P_{\text{cyto}} - \Big(k_{\text{off},P} + k_{PA} A^{\beta} \left[1 - \kappa_P\, F_P(\mathbf{r})\, f_P(t)\right] \Big) P, \tag{34}$$

$$R_M = k_{\text{on},M} M_{\text{cyto}} - \Big(k_{\text{off},M} \left[1 + \kappa_M\, F_M(\mathbf{r})\, f_M(t)\right] - k_{AM}\, A \Big) M. \tag{35}$$

Our experimental data is acquired in the mid-plane imaging geometry of the embryo. Assuming the entire polarization process has azimuthal symmetry about the anteroposterior axis of the embryo (*18*), we can simplify our theory by writing the dynamical equations in an elliptical cross-section of the embryo. This naturally leads us to consider periodic boundary conditions along the one-dimensional domain. Further, we neglect the curvature of the embryo (*12*) and finally consider our model on a one-dimensional line of size L with periodic boundary conditions.

The cytoplasmic concentration of a protein c (either A, P or M) in this one-dimensional theory is calculated from

$$c_{\text{cyto}} = c_{\text{tot}} - \frac{\psi}{L} \int_{-L/2}^{L/2} c(x,t)\, dx, \tag{36}$$

where ψ is the surface-to-volume ratio for the ellipsoidal geometry of the embryo, and $x \in [-L/2, L/2]$ with $x = 0$ corresponding to the posterior pole.

The total stress in the actomyosin cortex is given by

$$\sigma_{\text{tot}} = \eta\, \partial_x v + C_*\, f_C(t)\, \frac{M}{M+M_*}. \tag{37}$$

where η is the viscosity of the cortex (*4*). This together with the force-balance equation $\partial_x \sigma_{\text{tot}} = \gamma v$ leads to an equation for the cortical flows

$$\eta\, \partial_x^2 v - \gamma v = -C_*\, f_C(t)\, \partial_x \left(\frac{M}{M+M_*} \right). \tag{38}$$

Finally, the transport equations for A, P and M simplify to

$$\partial_t A = -\partial_x(vA) + D_A\partial_x^2 A + \frac{k_{\text{on},A}}{(1+k_{AP}P^\alpha)}A_{\text{cyto}} - k_{\text{off},A}\,A, \tag{39}$$

$$\partial_t P = -\partial_x(vP) + D_P\partial_x^2 P + k_{\text{on},P}P_{\text{cyto}} - \Big(k_{\text{off},P} + k_{PA}A^\beta\ \big[1-\kappa_P\,F_P(\mathbf{r})\,f_P(t)\big]\Big)\,P, \tag{40}$$

$$\partial_t M = -\partial_x(vM) + D_M\partial_x^2 M + k_{\text{on},M}M_{\text{cyto}} - \Big(k_{\text{off},M}\big[1+\kappa_M\,F_M(\mathbf{r})\,f_M(t)\big] - k_{AM}\,A\Big)\,M, \tag{41}$$

with

$$A_{\text{cyto}} = A_{\text{tot}} - \frac{\psi}{L}\int_{-L/2}^{L/2}dx A,\ P_{\text{cyto}} = P_{\text{tot}} - \frac{\psi}{L}\int_{-L/2}^{L/2}dx P,\ M_{\text{cyto}} = M_{\text{tot}} - \frac{\psi}{L}\int_{-L/2}^{L/2}dx M \tag{42}$$

and

$$F_P(x) = \exp\left(-\frac{x^2}{d_P^2}\right), \quad F_M(x) = \exp\left(-\frac{x^2}{d_M^2}\right), \tag{43}$$

$$f_P(t) = \frac{1}{2}\left[\tanh\left(\frac{t}{\tau_{P,\text{on}}}\right)+1\right], \tag{44}$$

$$f_M(t) = \frac{1}{2}\left[\tanh\left(\frac{t}{\tau_{M,\text{on}}}\right)-\tanh\left(\frac{t-T_M}{\tau_{M,\text{off}}}\right)\right], \tag{45}$$

$$f_C(t) = \frac{1}{2}\left[1-\tanh\left(\frac{t-T_M}{\tau_{M,\text{off}}}\right)\right]. \tag{46}$$

The above three transport equations (39, 40, 41) and the equation for the cortical flows (38) constitute our complete and self-consistent theory for PAR polarity in *C. elegans* embryos.

2.5 Numerical solutions of the model

Our theory as expressed by equations (38-46) cannot be solved analytically for the spatiotemporal evolution of the dynamical fields, even in the simplified one-dimensional geometry. As such, we resort to numerical methods to solve the partial differential equations.

We set up the problem in a one-dimensional line of size L in a periodic geometry. The position coordinate $x \in [-L/2, L/2]$ with the point $x = 0$ corresponding to the location of the posterior pole. The periodic boundary conditions, implied by as-

suming azimuthal symmetry and midplane imaging, leads us to solving the cortical flow equation (38) with high-precision spectral methods (*19*). We then discretize the transport equations (39, 40, 41) with finite-difference methods and use the method of lines employing accurate high-order time-marching algorithms to solve the resulting equations (*20*), using custom built code in Python (*21*).

2.6 Parameter inference procedure

At first sight, it appears that our theory has a large number of adjustable parameters. However, the values for many parameters are well known in the literature. Our data analysis procedures described in the Methods sections have led us to infer several more parameters. As such, there are only a moderate number of parameters which are unknown. See Supplementary Table S2 for a list of the known and unknown parameters. The main parameters that are unknown are those that pertain the characteristics of the triggering cues. Fortunately, the modularity of the PAR - actomyosin system allows us to determine these parameters, few at a time, in a systematic manner.

- *mlc-4* RNAi allows us to decouple the PAR patterning system from the NMY-2-flow system. This allows us to determine the parameters of the PAR-2 stabilization cue and the strengths of the mutual antagonistic interactions between the PARs.
- The *par-2* and *par-6* double RNAi condition isolates the NMY-2-flow system, thus allowing us to infer the characteristics of the myosin removal and contractility cue component.

For each of these two modular subsystems, we employ a systematic procedure to infer the set of unknown parameters, as described below.

2.6.1 Comparing theory and experimental data

For a given set of model parameters, our numeric evaluation returns the spatiotemporal profiles of the three concentration fields and the cortical velocity field, at any required space-time resolution. However, for a nonlinear theory, such as the present one, there is no direct and simple way to compare the theoretical solutions with experimental data to assess how good a given parameter set is. The standard reduced chi-squared measure can lead to erroneous results (*22*). As such, we used the following procedure to assess the agreement between the experimental data and the theoretical solution for a given set of input parameters.

Condition	Theoretical description
mlc-4 RNAi	$\partial_t A = -\partial_x(vA) + D_A\partial_x^2 A + \frac{k_{\text{on},A}}{(1+k_{AP}P^\alpha)}A_{\text{cyto}} - k_{\text{off},A}A,$ $\partial_t P = -\partial_x(vP) + D_P\partial_x^2 P + k_{\text{on},P}P_{\text{cyto}} - \left(k_{\text{off},P} + k_{PA}A^\beta\left[1-\kappa_P F_P(\mathbf{r})\, f_P(t)\right]\right)P,$ $\partial_t M = -\partial_x(vM) + D_M\partial_x^2 M + k_{\text{on},M}M_{\text{cyto}} - \left(k_{\text{off},M}\left[1+\kappa_M F_M(\mathbf{r})\, f_M(t)\right] - k_{AM}A\right)M,$ $\eta\partial_x^2 v - \gamma v = -C_*\, f_C(t)\,\partial_x\left(\frac{M}{M+M_*}\right)$
par-2 + *par-6* RNAi	$\partial_t A = -\partial_x(vA) + D_A\partial_x^2 A + \frac{k_{\text{on},A}}{(1+k_{AP}P^\alpha)}A_{\text{cyto}} - k_{\text{off},A}A,$ $\partial_t P = -\partial_x(vP) + D_P\partial_x^2 P + k_{\text{on},P}P_{\text{cyto}} - \left(k_{\text{off},P} + k_{PA}A^\beta\left[1-\kappa_P F_P(\mathbf{r})\, f_P(t)\right]\right)P,$ $\partial_t M = -\partial_x(vM) + D_M\partial_x^2 M + k_{\text{on},M}M_{\text{cyto}} - \left(k_{\text{off},M}\left[1+\kappa_M F_M(\mathbf{r})\, f_M(t)\right] - k_{AM}A\right)M,$ $\eta\partial_x^2 v - \gamma v = -C_*\, f_C(t)\,\partial_x\left(\frac{M}{M+M_*}\right)$
wt-MT$^-$	$\partial_t A = -\partial_x(vA) + D_A\partial_x^2 A + \frac{k_{\text{on},A}}{(1+k_{AP}P^\alpha)}A_{\text{cyto}} - k_{\text{off},A}A,$ $\partial_t P = -\partial_x(vP) + D_P\partial_x^2 P + k_{\text{on},P}P_{\text{cyto}} - \left(k_{\text{off},P} + k_{PA}A^\beta\left[1-\kappa_P F_P(\mathbf{r})\, f_P(t)\right]\right)P,$ $\partial_t M = -\partial_x(vM) + D_M\partial_x^2 M + k_{\text{on},M}M_{\text{cyto}} - \left(k_{\text{off},M}\left[1+\kappa_M F_M(\mathbf{r})\, f_M(t)\right] - k_{AM}A\right)M,$ $\eta\partial_x^2 v - \gamma v = -C_*\, f_C(t)\,\partial_x\left(\frac{M}{M+M_*}\right)$
unperturbed	$\partial_t A = -\partial_x(vA) + D_A\partial_x^2 A + \frac{k_{\text{on},A}}{(1+k_{AP}P^\alpha)}A_{\text{cyto}} - k_{\text{off},A}A,$ $\partial_t P = -\partial_x(vP) + D_P\partial_x^2 P + k_{\text{on},P}P_{\text{cyto}} - \left(k_{\text{off},P} + k_{PA}A^\beta\left[1-\kappa_P F_P(\mathbf{r})\, f_P(t)\right]\right)P,$ $\partial_t M = -\partial_x(vM) + D_M\partial_x^2 M + k_{\text{on},M}M_{\text{cyto}} - \left(k_{\text{off},M}\left[1+\kappa_M F_M(\mathbf{r})\, f_M(t)\right] - k_{AM}A\right)M,$ $\eta\partial_x^2 v - \gamma v = -C_*\, f_C(t)\,\partial_x\left(\frac{M}{M+M_*}\right)$

Table S1 – Table showing the equations used for different conditions.

- The experimental data fields $A_{\text{expt}}(x,t)$, $P_{\text{expt}}(x,t)$, $M_{\text{expt}}(x,t)$ and $v_{\text{expt}}(x,t)$ are arrays of shape $n_{\text{space}} \times n_{\text{time}}$ (Fig. 3a-c, h-j, main text). The theoretical solutions, $A_{\text{theory}}(x,t)$, $P_{\text{theory}}(x,t)$, $M_{\text{theory}}(x,t)$ and $v_{\text{theory}}(x,t)$, are also obtained at the same space-time resolution.

- We then order the space-time points in a sequence and compute the normalized residual array

$$\mathscr{R}_Z = \{\frac{Z_{\text{expt}}(x,t) - Z_{\text{theory}}(x,t)}{\sigma_{\text{expt}}(x,t)} \mid x,t\}, \qquad Z = \{A,P,M,v\} \tag{47}$$

  where $\sigma_{\text{expt}}(x,t)$ is the experimental standard error of the mean for the variable Z at the point (x,t). Note that for each field Z, the array $\mathscr{R}_Z$ is a one-dimensional vector of length $n_{\text{space}} \times n_{\text{time}}$.

- For multiple fields, we collate the residual arrays into a single residual array $\mathscr{R} = \{\mathscr{R}_A, \mathscr{R}_P, \mathscr{R}_M, \mathscr{R}_v\}$.

- If the deviation of the data from the theoretical model is entirely due to statistical fluctuations, then the array $\mathscr{R}$ should have a normal distribution with zero mean and unit variance. We thus calculate, for each condition the two quantities (mean: $\mathscr{R}_{\text{mean}}$, variance: $\mathscr{R}_{\text{variance}}$) to characterize the goodness of the fit.

- As a goodness of fit test, we compare the normalized histogram of the array $\mathscr{R}$ with a normal distribution. To get a quantitative estimate of the comparison, we generate the quantile plots for the residual array $\mathscr{R}$ against a standard normal distribution. In the ideal case, this plot would be a straight line with unit slope and zero intercept (Supplementary Fig. 14).

In order to obtain good estimates of the four parameters ($k_{\text{on},A}, k_{\text{on},P}, k_{AP}, k_{PA}$) of the non-linear PAR reaction network and the strength of the PAR-2 stabilization cue (κ_P), we applied a fitting procedure where we first systematically evaluated a cost function, which quantifies the agreement of the theoretical solution with the experimental data, over a large range of parameter values. We systematically explored a broad range of combinations of the 5 parameters and compared the theoretical solution to the experimental data. For this comparison, we used the cost function

$$\text{cost} = \ (\mathscr{R}_{\text{variance}} - 1) \ + \ |\mathscr{R}_{\text{mean}}|, \tag{48}$$

for which each term is zero when the deviation of the data from the theoretical model is entirely due to statistical fluctuations. We evaluated the cost function for both, of the *mlc-4* RNAi condition and the PAR-2 MT- condition. For the *mlc-4* RNAi condition, flows are inhibited, while for the PAR-2 MT- condition, the PAR-2 stabilization cue is inhibited, such that both conditions provide relatively simple cases that cover a broad spectrum of phenotypes. To obtain a good estimate for $k_{\text{on},A}, k_{\text{on},P}, k_{AP}, k_{PA}$ and κ_P, we used:

$$\text{cost} = \ \frac{1}{2}(\text{cost}_{mlc4} + \text{cost}_{\text{PAR2MT}-}). \tag{49}$$

For each condition, we focused on parameter regions in which the homogeneous A-high state is stable (evaluated by linear stability analysis) and the PAR biochemistry shows multistability (the P and A nullclines have more than one intersection point). For instance, Supplementary Fig. 13 shows a heat map of this cost function for the *mlc-4* RNAi condition in some plane. We determined the global minimum of the cost function over this grid of 5 parameters to obtain an optimal starting parameter set. This parameter set, in combination with estimates for the width d_P and the switching time

$\tau_{P,\mathrm{on}}$ was then used as a starting point for a least squares minimization procedure using the Levenberg-Marquardt fitting algorithm. For the NMY-2-flow system, only 4 parameters were unknown (Supplemental Table S2 andS3) and for good convergence it was sufficient to use manual estimates as starting values for the least squares minimization procedure using the Levenberg-Marquardt fitting algorithm. We used the python library 'lmfit' to perform this final stage of the fitting procedure (*23*). This procedure also gives us estimates of the uncertainties (1σ) in the inferred parameters, from which we calculate and report the 95% confidence intervals. Note, however, that the estimates of the 95% confidence intervals from such a fitting procedure are generally not very robust and should be treated with caution (*22*).

2.6.2 Sensitivity analysis

We used a one-variable-at-a-time method to evaluate the sensitivity of our model solution to changes in the values of all parameters. For that, we varied one of our model parameters, while keeping the other parameters fixed to the values in Supplementary Table S2. We increased as well as decreased each parameter value. Then we evaluated the change in the solution by the following distance function. Let A_0, P_0, M_0 and v_0 be the solutions for the unperturbed condition. Let $A_{h/l}, P_{h/l}, M_{h/l}$ and $v_{h/l}$ be the concentration and flow fields for the variation of one parameter (high or low).
Then we define the distance measure for the unperturbed condition as:

$$\frac{1}{4}\Big(\frac{\int_{x,t}(A_0-A_{h/l})^2dxdt}{\int_{x,t}A_0^2dxdt}+\frac{\int_{x,t}(P_0-P_{h/l})^2dxdt}{\int_{x,t}P_0^2dxdt}+\frac{\int_{x,t}(M_0-M_{h/l})^2dxdt}{\int_{x,t}M_0^2dxdt}+\frac{\int_{x,t}(v_0-v_{h/l})^2dxdt}{\int_{x,t}v_0^2dxdt}\Big) \quad (50)$$

The distance value is zero for identical concentration fields in A, P and M and flow fields v. The distance is expressed as variance and normalized by the mean (Supplementary Fig. 12). We find that less than 30 percent of the parameters have a significant impact on the solutions. The most impactful parameters control the anterior PAR proteins and thus the stability of the initial, homogeneous state.

2.7 Linear stability analysis for the PAR-myosin-flow system

The PAR biochemical reactions represented by the equations (23) and (24) exhibit bistability for $\alpha \geq 1, \beta > 1$ or $\alpha > 1, \beta \geq 1$ (*12, 13*). For the best set of parameters determined for the unperturbed condition, the nullclines $R_A = 0$ and $\tilde{R}_P = 0$ defined by equation (23) and (24) have three possible solutions for the uniform steady-states of the PAR system, represented by three intersection points. It turns out that the aPAR domi-

nant state and the pPAR dominant state are stable, but the third state is unstable (*12,13*). Additionally, the parameters corresponding the aPAR dominant state also allow the existence of polarized domain states, giving rise to coexistence of stable solutions. In the coexistence region, both the homogeneous state and the polarized domain state are stable to small fluctuations. A large perturbation, exceeding a certain threshold, is required to drive the system from the homogeneous state to the domain state. The *C. elegans* zygote is initially in the homogeneous aPAR dominant state and is driven by the cues to the polarized domain state. We next study the stability of the aPAR dominant homogeneous state to small non-uniform perturbations, in the presence of active mechanics, promoted by the NMY-2 concentration field.

We consider the PAR - actomyosin system without the external cues

$$\partial_t A = -\partial_x(vA) + D_A\partial_x^2 A + \frac{k_{\text{on},A}}{(1+k_{AP}P^\alpha)}A_{\text{cyto}} - k_{\text{off},A}\,A, \tag{51}$$

$$\partial_t P = -\partial_x(vP) + D_P\partial_x^2 P + k_{\text{on},P}P_{\text{cyto}} - \left(k_{\text{off},P} + k_{PA}A^\beta\right)P, \tag{52}$$

$$\partial_t M = -\partial_x(vM) + D_M\partial_x^2 M + k_{\text{on},M}M_{\text{cyto}} - \left(k_{\text{off},M} - k_{AM}\,A\right)M, \tag{53}$$

$$\eta\,\partial_x^2 v - \gamma v = -C_*\,\partial_x\left(\frac{M}{M+M_*}\right). \tag{54}$$

and investigate the stability of the homogeneous state with respect to small perturbations in the concentrations of the PARs and myosin. The above equations have a unique homogeneous steady-state, $\mathbf{c}_0 = (A_0, P_0, M_0)$, which is obtained by solving the following equations in a self-consistent manner:

$$A_0 = \frac{k_{\text{on},A}\,A_{\text{tot}}}{k_{\text{on},A}\,\psi + k_{\text{off},A} + k_{AP}\,P_0^\alpha}, \tag{55}$$

$$P_0 = \frac{k_{\text{on},P}\,P_{\text{tot}}}{k_{\text{on},P}\,\psi + k_{\text{off},P} + k_{PA}\,A_0^\beta}, \tag{56}$$

$$M_0 = \frac{k_{\text{on},M}\,M_{\text{tot}}}{k_{\text{on},M}\,\psi + k_{\text{off},M} - k_{AM}\,A_0}. \tag{57}$$

Following (*24*), the linear stability matrix, for a perturbation of the form e^{iqx} around the homogeneous steady-state $\mathbf{c}_0$, is

$$\mathscr{A}_{ij} = -q^2\,D_i\,\delta_{ij} + C_*\,\frac{q^2}{1+q^2\ell^2}\;\; c_{i,0}\;\partial_{c_j}f(\mathbf{c}_0) + \partial_{c_j}R_i(\mathbf{c}_0) \tag{58}$$

where $i = \{A, P, M\}$. We get

$$\mathscr{A} = -q^2 \begin{pmatrix} D_A & 0 & 0 \\ 0 & D_P & 0 \\ 0 & 0 & D_M \end{pmatrix} \quad + \quad C_* \frac{q^2}{1+q^2\ell^2} \frac{M_*}{(M_0+M_*)^2} \begin{pmatrix} 0 & 0 & A_0 \\ 0 & 0 & P_0 \\ 0 & 0 & M_0 \end{pmatrix}$$

$$+ \begin{pmatrix} -k_{\mathrm{off},A} - \frac{\psi k_{\mathrm{on},A}\delta_{q,0}}{(1+k_{AP}P_0^\alpha)} & -\frac{k_{\mathrm{on},A}(A_{\mathrm{tot}} - \psi A_0 \delta_{q,0})}{(1+k_{AP}P_0^\alpha)^2} \alpha k_{AP} P_0^{\alpha-1} & 0 \\ -\beta k_{PA} A_0^{\beta-1} P_0 & -k_{\mathrm{off},P} - \psi k_{\mathrm{on},P}\delta_{q,0} - k_{PA}A_0^\beta & 0 \\ k_{AM} M_0 & 0 & -k_{\mathrm{off},M} - \psi k_{\mathrm{on},M}\delta_{q,0} - k_{AM}A_0 \end{pmatrix} \tag{59}$$

The eigenvalues of the above linear stability matrix determine whether the homogeneous state is stable to a small non-uniform perturbation. We numerically compute the eigenvalues using the best-fit parameters for the unperturbed condition (Table S2), and plot it as a function of the wavenumber q of the perturbation. If the eigenvalues for all spatial modes are smaller than zero, the homogeneous aPAR dominated state is stable. For Fig. 4b, main text, we explored a large range of values for k_{AM} and C_* and evaluated if the corresponding eigenvalues for all spatial modes of infinitesimally small perturbations remained negative. This then represents the region where the homogeneous state is stable. We furthermore simulated the PAR - actomyosin system, using the unperturbed-condition parameters, while k_{AM} and C_* were varied. As shown in Fig. 2b, main text, the PAR-2 stabilization cue causes PAR domain formation even in the absence of cortical flows. In order to investigate the perturbation originating from cortical flows, in their propensity to trigger domain formation, we numerically inactivated the PAR-2 stabilization cue by setting κ_P to zero. We then numerically evaluated if the perturbation of cortical flows triggers domain formation. In Fig. 4b, main text, the grey region indicates the parameter range, for which the advective polarity trigger fails to establish PAR domains.

2.8 Correlations in the concentration fields

In Supplementary Fig. 15, we plot the spatiotemporal normalized crosscorrelation functions (*25*) for the concentration fields of PAR-2, PAR-6 and NMY-2. The correlations obtained from the experimental data show negative correlation between PAR-2 and PAR-6 as well as NMY-2 and PAR-2 in the domain region and positive correlation between NMY-2 and PAR-6. For the parameter values of the unperturbed condition (Supplementary Table S2,S3), we plotted the correlation functions predicted from our

theory of guided mechanochemical self-organization. From this comparison it becomes evident that the agreement between theory and experiment is reasonably good, even at the quantitative level. Our mechanochemical theory of guided self-organization is a coarse-grained description of the microscopic dynamics. We have not included any stochastic fluctuations in our equations for the dynamics of the concentration fields, as coarse-grained theories average out stochastic fluctuations. The experimental *C. elegans* zygote of course exhibits stochastic fluctuations arising from various sources. Despite this fact, the correlation functions computed from experimental and the theoretical predictions still agree with each very well. This indicates that our theory is able to capture the dynamics of the system even beyond the simple mean-field level.

3 Supplementary Tables

parameter	known?	source	value
$k_{\text{on},A}$	x	fitting$^{(*)}$	$(2.115\pm0.008)\cdot10^{-2}\ \mu m s^{-1}$
$k_{\text{off},A}$	✓	(*10*)	$(9.2\pm2)\ \cdot10^{-3}s^{-1}$
$k_{\text{on},P}$	x	fitting$^{(*)}$	$(1.3012\pm0.0006)\cdot10^{-1}\mu m s^{-1}$
$k_{\text{off},P}$	✓	(*3*)	$(7.3\pm5.7)\cdot10^{-3}s^{-1}$
$k_{\text{on},M}$	✓	Fig. 1d	$0.199\pm0.04\mu m s^{-1}$
$k_{\text{off},M}$	✓	Fig. 1c	$0.117\pm0.009s^{-1}$
D_A	✓	(*10*)	$0.095\pm0.04\mu m^2 s^{-1}$
D_P	✓	(*3*)	$0.15\pm0.03\mu m^2 s^{-1}$
D_M	✓	Supplementary Fig. 4c	$0.054\pm0.003\mu m^2 s^{-1}$
ρ_A	✓	MACE, Supplementary Fig. 3i,j,l,m	see table S3
ρ_P	✓	MACE, Supplementary Fig. 3i,j,l,m	see table S3
ρ_M	✓	MACE, Supplementary Fig. 3i,j,l,m	see table S3
k_{PA}	x	fitting$^{(*)}$	$(1.318\pm0.0007)\cdot10^{-2}\mu m^4 s^{-1}$
k_{AP}	x	fitting$^{(*)}$	$1.11\pm0.017\mu m^2$
α	✓	(*12*)	1
β	✓	(*12*)	2
k_{AM}	✓	Fig. 1c	-$(2.0\pm0.7)\ \cdot10^{-3}\mu m^2 s^{-1}$
l	✓	(*26*)	$13.6\pm2.9\mu m$
C_*/γ	x	fitting$^{(*)}$	$10.4\pm\ 1.0Nm$
M_*	x	fitting$^{(*)}$	$8.0\pm\ 4.9\ \mu\text{m}^{-2}$
κ_M	x	fitting$^{(*)}$	4.9 ± 0.3
d_M	x	fitting$^{(*)}$	$15.9\ \pm0.6\mu m$
T_M	✓	Supplementary Fig. 6	see table S3
$\tau_{M,\text{on}}$	✓	Supplementary Fig. 6	see table S3
$\tau_{M,\text{off}}$	✓	Supplementary Fig. 6	see table S3
κ_P	x	fitting$^{(*)}$	0.951 ± 0.0006
d_P	x	fitting$^{(*)}$	$28.6\pm0.16\mu m$
$\tau_{P,on}$	x	fitting$^{(*)}$	$74\pm4.4s$

Table S2 – Parameter values of the physical model for the dynamics of PAR polarity establishment. $^{(*)}$: Errors represent the 95% confidence interval. Note however that this can be an underestimation of the real error, due to the nature of the fitting routine (see SI section 2.6.1).

condition	$\rho_A\ [\mu m^{-3}]$	$\rho_P\ [\mu m^{-3}]$	$\rho_M\ [\mu m^{-3}]$	$\tau_{M,\mathrm{on}}\ [s]$	$\tau_{M,\mathrm{off}}\ [s]$	$T_M\ [s]$
unperturbed	9.18 ± 0.50	6.30 ± 0.40	13.1 ± 0.9	32 ± 10	89 ± 19	322 ± 11
par-2 par-6 RNAi	4.03 ± 0.15	2.14 ± 0.17	14.1 ± 0.8	36 ± 11	99 ± 18	204 ± 10
par-6 RNAi	2.8 ± 0.25	6.0 ± 0.35	11.8 ± 0.6	29 ± 14	100 ± 25	185 ± 14
mlc-4 RNAi	9.22 ± 0.50	4.95 ± 0.37	–	–	–	–
PAR-2 MT- mutant	8.71 ± 0.45	4.02 ± 0.22	15.6 ± 0.9	32 ± 14	112 ± 30	403 ± 17

Table S3 – Table of condition-dependent parameter-values. Errors represent the 95% confidence interval.

NMY-2 GFP	LP133	*nmy-2(cp8[NMY-2::GFP + unc-119(+)]) I; unc-119(ed3) III*
NMY-2 mKate2	LP229	*nmy-2(cp52[nmy-2::mkate2 + LoxP unc-119(+) LoxP]) I; unc-119(ed3) III*
PH-Domain mCherry	OD70	*ltIs44pAA173; [pie-1p-mCherry::PH(PLC1delta1) + unc-119(+)]*
PH-Domain GFP	OD58	*ltIs38[pAA1; pie-1::GFP::PH(PLC1delta1) + unc-119(+)]*
PAR-2 MT- GFP	JH2815	*unc-119(ed3); axIs1934[pFM035 gfp::par-2$^{RNAi-resistant}$ [R183-5A]]*
PAR-2 GFP	TH129	*unc-119(ed3)III; ddIs25[[pie-1p::GFP::F58B6.3;unc-119(+)]*
PAR-6 mCherry	TH110	*unc-119(ed3)III; ddIs26[mCherry::T26E3.3;unc-119(+)]*
NMY-2 GFP PH-Domain mCherry	SWG070	cross between LP133 and OD70
NMY-2 mKate2 PAR-2 MT- GFP	SWG021	cross between LP229 and JH2815
PAR-2 MT- GFP PAR-6 mCherry	SWG025	cross between JH2815 and TH110
PAR-2 GFP PAR-6 mCherry	TH120	cross between TH129 and TH110
PAR-2 mNeonGreen SPD-5 GFP	SWG142	cross between SWG143 and OD847

Table S4 – *C. elegans* strains, used in this study.

References

1. François B Robin, Jonathan B Michaux, William M McFadden, and Edwin M Munro. Excitable rhoa dynamics drive pulsed contractions in the early c. elegans embryo. *bioRxiv*, 2016.

2. Masatoshi Nishikawa, Sundar Ram Naganathan, Frank Juelicher, and Stephan W. Grill. Controlling contractile instabilities in the actomyosin cortex. *eLife*, 6, JAN 28 2017.

3. Nathan W. Goehring, Carsten Hoege, Stephan W. Grill, and Anthony A. Hyman. PAR proteins diffuse freely across the anterior-posterior boundary in polarized C. elegans embryos. *Journal of Cell Biology*, 193(3):583–594, MAY 2 2011.

4. Mirjam Mayer, Martin Depken, Justin S. Bois, Frank Juelicher, and Stephan W. Grill. Anisotropies in cortical tension reveal the physical basis of polarizing cortical flows. *Nature*, 467(7315):617–U150, SEP 2010.

5. Bob Goldstein and Ian G. Macara. The PAR proteins: Fundamental players in animal cell polarization. *Developmental Cell*, 13(5):609–622, NOV 2007.

6. B Etemadmoghadam, S Guo, and KJ Kemphues. Asymmetrically distributed PAR-3 protein contributes to cell polarity and spindle alignment in early *C. elegans* embryos. *Cell*, 83(5):743–752, DEC 1 1995.

7. L Boyd, S Guo, D Levitan, DT Stinchcomb, and KJ Kemphues. PAR-2 is asymmetrically distributed and promotes association of P granules and PAR-1 with the cortex in C. elegans embryos. *Development*, 122(10):3075–3084, OCT 1996.

8. R Benton and D St Johnston. Drosophila PAR-1 and 14-3-3 inhibit Bazooka/PAR-3 to establish complementary cortical domains in polarized cells. *Cell*, 115(6):691–704, DEC 12 2003.

9. YS Hao, L Boyd, and G Seydoux. Stabilization of cell polarity by the C. elegans RING protein PAR-2. *Developmental Cell*, 10(2):199–208, FEB 2006.

10. Francois B. Robin, William M. McFadden, Baixue Yao, and Edwin M. Munro. Single-molecule analysis of cell surface dynamics in Caenorhabditis elegans embryos. *Nature Methods*, 11(6):677+, JUN 2014.

11. Anne Sailer, Alexander Anneken, Younan Li, Sam Lee, and Edwin Munro. Dynamic Opposition of Clustered Proteins Stabilizes Cortical Polarity in the C. elegans Zygote. *Developmental Cell*, 35(1):131–142, OCT 12 2015.

12. Nathan W. Goehring, Philipp Khuc Trong, Justin S. Bois, Debanjan Chowdhury, Ernesto M. Nicola, Anthony A. Hyman, and Stephan W. Grill. Polarization of PAR Proteins by Advective Triggering of a Pattern-Forming System. *Science*, 334(6059):1137–1141, NOV 25 2011.

13. Philipp Khuc Trong, Ernesto M. Nicola, Nathan W. Goehring, K. Vijay Kumar, and Stephan W. Grill. Parameter-space topology of models for cell polarity. *New Journal Of Physics*, 16, JUN 13 2014.

14. Sungrim Seirin Lee and Tatsuo Shibata. Self-organization and advective transport in the cell polarity formation for asymmetric cell division. *Journal of Theoretical Biology*, 382:1–14, 2015.

15. Fumio Motegi, Seth Zonies, Yingsong Hao, Adrian A. Cuenca, Erik Griffin, and Geraldine Seydoux. Microtubules induce self-organization of polarized PAR domains in Caenorhabditis elegans zygotes. *Nature Cell Biology*, 13(11):1361–U171, 2011.

16. Fumio Motegi and Asako Sugimoto. Sequential functioning of the ECT-2 RhoGEF, RHO-1 and CDC-42 establishes cell polarity in Caenorhabditis elegans embryos. *Nature Cell Biology*, 8(9):978–U80, 2006.

17. Yu Chung Tse, Michael Werner, Katrina M. Longhini, Jean-Claude Labbe, Bob Goldstein, and Michael Glotzer. RhoA activation during polarization and cytokinesis of the early Caenorhabditis elegans embryo is differentially dependent on NOP-1 and CYK-4. *Molecular Biology of the Cell*, 23(20):4020–4031, 2012.

18. Lesilee Rose and Pierre Gönczy. Polarity establishment, asymmetric division and segregation of fate determinants in early C. elegans embryos. *WormBook*, pages 1–43, December 2014.

19. Lloyd N. Trefethen. *Spectral Methods in MATLAB (Software, Environments, Tools)*. SIAM: Society for Industrial and Applied Mathematics, 2 2001.

20. Willem Hundsdorfer and Jan G. Verwer. *Numerical Solutions of Time-Dependent Advection-Diffusion-Reaction Equations*. Springer, 2007.

21. Python software foundation. http://www.python.org.

22. R. Andrae, T. Schulze-Hartung, and P. Melchior. Dos and don'ts of reduced chi-squared. *ArXiv e-prints*, December 2010.

23. Matthew Newville, Till Stensitzki, Daniel B. Allen, and Antonino Ingargiola. LMFIT: Non-Linear Least-Square Minimization and Curve-Fitting for Python, September 2014.

24. Justin S. Bois, Frank Jülicher, and Stephan W. Grill. Pattern Formation in Active Fluids. *Physical Review Letters*, 106(2), 2011.

25. D Padfield. Masked Object Registration in the Fourier Domain. *IEEE Transactions on Image Processing*, 21(5):2706–2718, 2012.

26. Arnab Saha, Masatoshi Nishikawa, Martin Behrndt, Carl-Philipp Heisenberg, Frank Jülicher, and Stephan W. Grill. Determining Physical Properties of the Cell Cortex. *Biophysical Journal*, 110(6):1421–1429, 2016.

27. William Thielicke and Eize J. Stamhuis. PIVlab - Time-Resolved Digital Particle Image Velocimetry Tool for MATLAB. 07 2014.

Supplementary Movie Legends

Movie S1. Concentration field of PAR-2::GFP (blue, N = 8) and PAR-6::mCherry (red, N = 8), during *mlc-4* RNAi, over time. Error bands represent the standard error of the mean. The solid line shows the best fit, using equations as described in table S1, with parameters shown in tables S2 and S3.

Movie S2. Ensemble-averaged concentration field of NMY-2::GFP (grey, N = 8) and the ensemble-averaged NMY-2 flow field (green, N = 10), during *par-2* and *par-6* double RNAi, over time. Error bands represent the standard error of the mean. The solid line shows the best fit, using equations as described in table S1, with parameters shown in tables S2 and S3.

Movie S3. Ensemble-averaged concentration field of PAR-2-MT-::GFP (blue, N = 9) and PAR-6::mCherry (red, N = 9) NMY-2::mKate2 (grey, N = 6) and the ensemble-averaged NMY-2 flow field (green, N = 9) for the PAR-2 MT- condition, over time. Error bands represent the standard error of the mean. The solid line shows the model prediction, using equations as described in table S1, with parameters shown in tables S2 and S3.

Movie S4. Ensemble-averaged concentration field of PAR-2::GFP (blue, N = 6) and PAR-6::mCherry (red, N = 6) NMY-2::GFP (grey, N = 8) and the ensemble-averaged NMY-2 flow field (green, N = 12) for the unperturbed condition, over time. Error bands represent the standard error of the mean. The solid line shows the model prediction, using equations as described in table S1, with parameters shown in tables S2 and S3.

Movie S5. Ensemble-averaged concentration field of PAR-2::GFP (blue, N = 6) and PAR-6::mCherry (red, N = 6) NMY-2::GFP (grey, N = 8) and the ensemble-averaged NMY-2 flow field (green, N = 12) for the unperturbed condition, over time. Error bands represent the standard error of the mean. The solid line shows a fit to the model, using equations as described in table S1, as shown in Supplementary Fig. 9.

Supplementary Figures

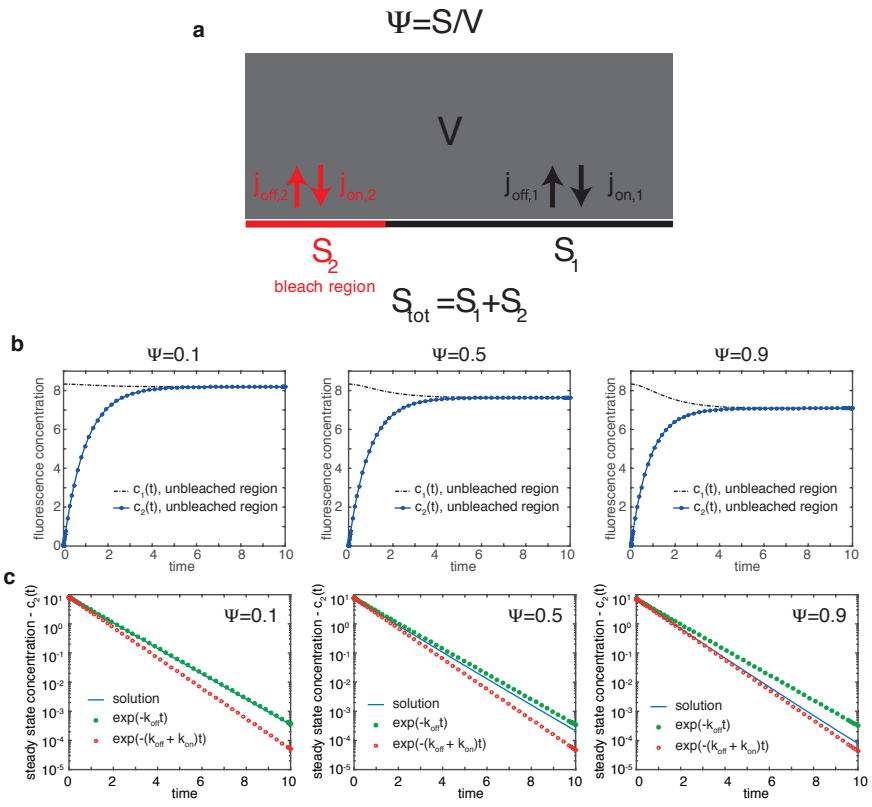

Fig. S1 – FRAP as method to measure dissociation rates. a, FRAP geometry. The membrane consists out of a region S_1, which is not bleached, and a region S_2, where the bleaching event has taken place. We consider $\gamma = S_2/S_{tot}$ as the fraction of the bleached to the total surface area. Both regions are coupled to the cytoplasm V. **b**, Concentrations of fluorescence particles on the membrane, after the FRAP event. First row: Dynamics of the concentration at the bleached region (blue, S2) and the unbleached region (black, S1) as a function of γ, which gives the ratio of the bleached region to the total surface area. Second row: The solution of the concentration of the bleached region minus the steady state, on a log plot, also for the three different γ values (0.1, 0.5, 0.9). Also plotted are the dynamics of the two eigenvalues, $\lambda_1 = -k_{off} - k_{on}\psi$ and $\lambda_2 = -k_{off}$, as a guide to the eye. All three conditions used: $k_{on} = 1$, $k_{off} = 1$, $\psi = 0.2$, $\rho_{total} = 10$.

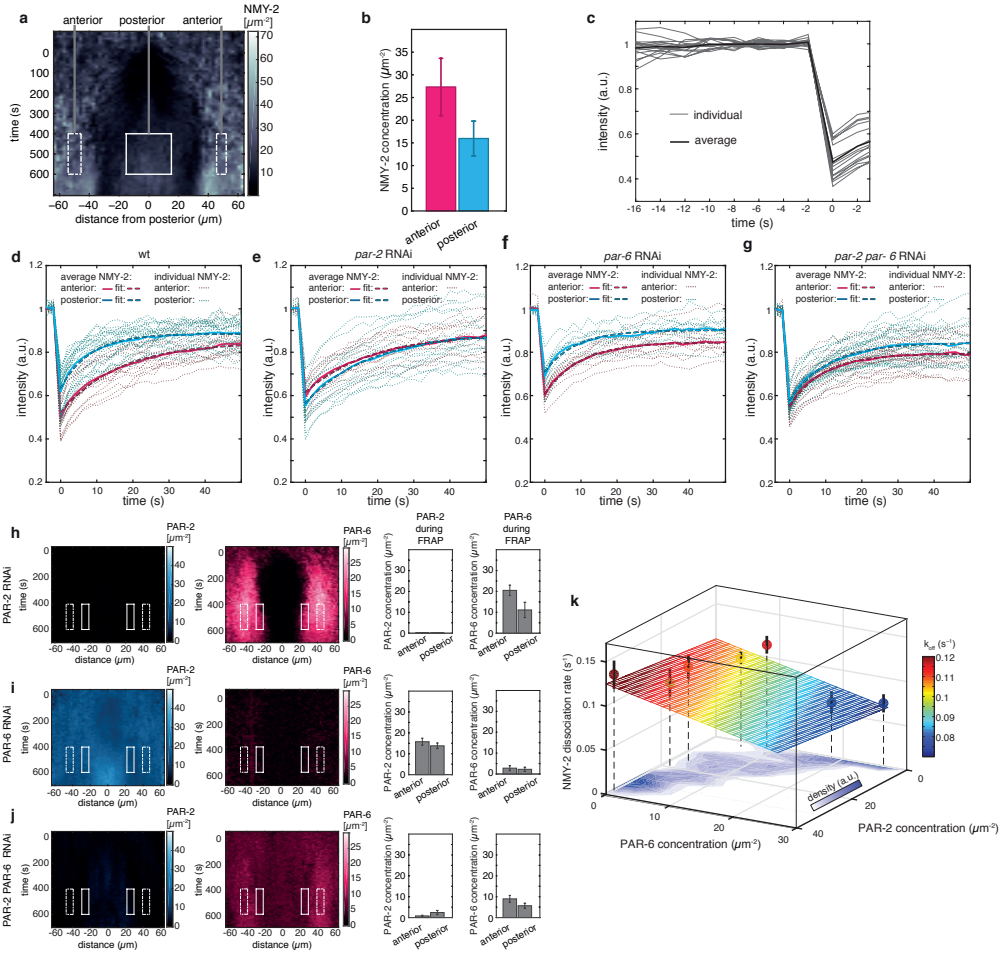
a
anterior
posterior
anterior
NMY-2 [μm⁻²]
time (s)
distance from posterior (μm)
b
NMY-2 concentration (μm⁻²)
anterior
posterior
c
intensity (a.u.)
individual
average
time (s)
d
wt
e
par-2 RNAi
f
par-6 RNAi
g
par-2 par- 6 RNAi
average NMY-2:
individual NMY-2:
anterior:
posterior:
fit:
intensity (a.u.)
time (s)
h
PAR-2 RNAi
PAR-6 [μm⁻²]
PAR-2 during FRAP
PAR-6 during FRAP
PAR-2 concentration (μm⁻²)
PAR-6 concentration (μm⁻²)
distance (μm)
i
PAR-6 RNAi
j
PAR-2 PAR-6 RNAi
k
NMY-2 dissociation rate (s⁻¹)
PAR-6 concentration (μm⁻²)
PAR-2 concentration (μm⁻²)
density (a.u.)
k_off (s⁻¹)

Fig. S2 – NMY-2 dissociation rate as a function of the PAR concentration. **a**, Spatiotemporal concentration profile of NMY-2 (see Fig. 3i, main text, N=8) during fluorescence recovery after photobleaching (FRAP). FRAP was performed in a time period where the NMY-2 levels were close to steady state. To determine the average concentration of NMY-2 during the FRAP events, we calculated the mean and standard deviation in a time interval between 400s and 600s after polarity triggering. We defined the posterior region as an interval between -15 µm and 15 µm. The anterior region was defined as $\pm$ 45 µm to $\pm$ 55 µm. **b**, Average NMY-2 concentration and standard deviation in the anterior and posterior domain, using panel a (N=8). **c**, The NMY-2 concentration prior to the FRAP event reached a steady state (anterior, N=16). Light grey: individual NMY-2 concentrations. Dark grey: averaged NMY-2 concentration. Individual and averaged FRAP recovery of NMY-2 both in the anterior (red) and in the posterior (cyan) hemisphere, displayed for the four conditions: **d**, unperturbed (anterior: N=16, posterior: N=24), **e**, *par-2* RNAi (anterior: N=11, posterior: N=15), **f**, *par-6* RNAi (anterior: N=12, posterior: N=9), **g**, *par-2* + *par-6* RNAi (anterior: N=26, posterior: N=24). Fitting the fluorescence recovery provided the NMY-2 dissociation rates, shown in Fig. 1b, main text. Concentration of PAR proteins during FRAP experiments for various RNAi perturbations: spatiotemporal profile of PAR-2, PAR-6, as well as PAR-2 and PAR-6 concentration and standard deviation in the anterior (dashed rectangle) and posterior domain (rectangle) for **h**, *par-2* RNAi (N=7), **i**, *par-6* RNAi (N=6) and **j**, *par-2 par-6* double RNAi (N=10). The distance of the FRAP region to the posterior pole was determined prior to each individual FRAP event, yielding $d = 43.3\pm$ 2.6 µm for anterior FRAP and $d = 25.6\pm$ 2.8 µm for posterior FRAP, as average distance. **k**, NMY-2 dissociation rates, measured by FRAP (Fig. 1b,c, main text), plotted against the respective PAR-2 and PAR-6 concentrations. Error bars are standard error of the mean. Note that we excluded k_{diss} during *par-2* RNAi in the posterior domain, since small uncertainties in the FRAP position can have a strong impact on the PAR-6 concentration, which is thus difficult to asses. We fitted the dissociation rate with a linear relation $k_{\text{diss}} = k_{\text{off},M} + k_{AM}A + k_{PM}P$, and inferred $k_{AM} = -0.0016 \pm 0.0023$ µm^{2}s^{-1}, $k_{PM} = 3.6\text{e}-04 \pm 0.001.9$ µm^{2}s^{-1} and $k_{\text{off},M} = 0.16 \pm 0.002$ s^{-1}.

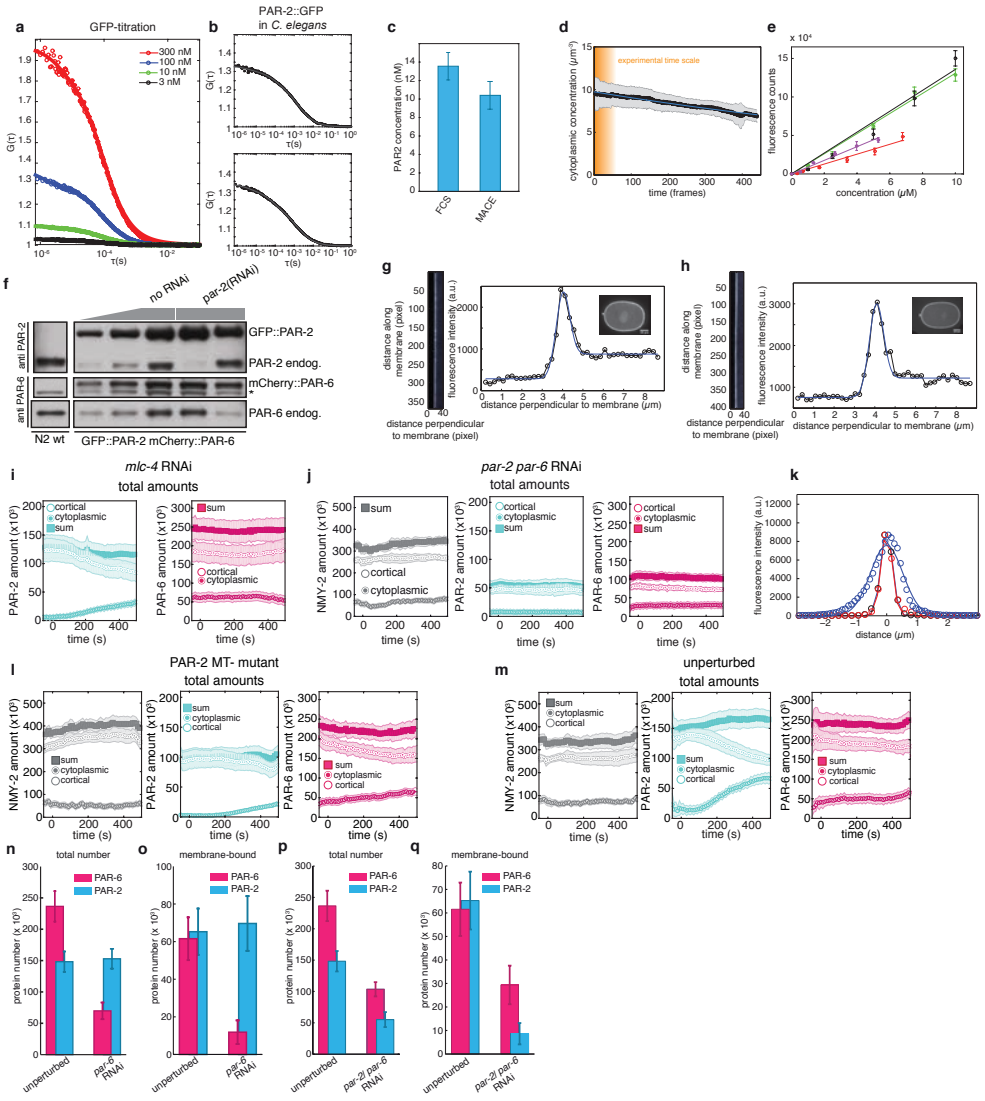
a
GFP-titration
300 nM
100 nM
10 nM
3 nM
G(τ)
τ(s)
b
PAR-2::GFP
in C. elegans
c
PAR2 concentration (nM)
FCS
MACE
d
experimental time scale
cytoplasmic concentration (μm⁻³)
time (frames)
e
x 10⁴
fluorescence counts
concentration (μM)
f
no RNAi
par-2(RNAi)
anti PAR-2
anti PAR-6
GFP::PAR-2
PAR-2 endog.
mCherry::PAR-6
*
PAR-6 endog.
N2 wt
GFP::PAR-2 mCherry::PAR-6
g
distance along membrane (pixel)
fluorescence intensity (a.u.)
distance perpendicular to membrane (μm)
distance perpendicular to membrane (pixel)
h
distance along membrane (pixel)
fluorescence intensity (a.u.)
distance perpendicular to membrane (μm)
distance perpendicular to membrane (pixel)
i
mlc-4 RNAi
total amounts
cortical
cytoplasmic
sum
PAR-2 amount (x10⁶)
PAR-6 amount (x10⁶)
time (s)
j
par-2 par-6 RNAi
total amounts
NMY-2 amount (x10⁶)
PAR-2 amount (x10⁶)
PAR-6 amount (x10⁶)
time (s)
k
fluorescence intensity (a.u.)
distance (μm)
l
PAR-2 MT- mutant
total amounts
NMY-2 amount (x10⁶)
PAR-2 amount (x10⁶)
PAR-6 amount (x10⁶)
time (s)
m
unperturbed
total amounts
NMY-2 amount (x10⁶)
PAR-2 amount (x10⁶)
PAR-6 amount (x10⁶)
time (s)
n
total number
PAR-6
PAR-2
protein number (x 10⁶)
unperturbed
par-6 RNAi
o
membrane-bound
PAR-6
PAR-2
protein number (x 10⁶)
unperturbed
par-6 RNAi
p
total number
PAR-6
PAR-2
protein number (x 10⁶)
unperturbed
par-2 par-6 RNAi
q
membrane-bound
PAR-6
PAR-2
protein number (x 10⁶)
unperturbed
par-2 par-6 RNAi

Fig. S3 – Protein concentrations measured by MACE. a, FCS autocorrelation spectra for GFP in solution, with 4 different concentrations (300 nM, 100 nM, 10 nM, 3 nM). Quantitative analysis yielded $V_{\mathrm{conf}} = 3.3e^{-16} \pm 3e^{-17}$ liters. **b**, Two individual FCS autocorrelation spectra for PAR-2::GFP in living *C. elegans* zygotes (circles). Black line: Theoretical fit, yielding a diffusive time-scale of $\tau_D = 98.5$ μs and $\tau_D = 77.5$ μs. **c**, Comparing the PAR-2 concentration of *C. elegans* one-cell zygotes, determined via FCS (13.6 ± 1.5 nM, N=21) with the quantity determined via MACE (10.4 ± 1.5 nM, N=8). **d**, Photobleaching during image-acquisition, for cytoplasmic NMY-2::GFP concentration (N=6) Error: Standard deviation. Blue line: exponential fit yielding a bleaching time scale of t_{bleach} = 1428 frames. **e:** Fluorescence calibration curves of GFP (green), mCherry (red), mNeonGreen (magenta) and mKate2 (black). Error bars: Standard deviation. The solid line shows a linear fit (see Methods). **f**, The ratio of labeled to unlabelled PAR-2 and PAR-6. Left side: Western blot against PAR-2 and PAR-6 for the N2 wt line. Right side: Western blot against PAR-2 and PAR-6 for the PAR-2::GFP and PAR-6::mCherry transgenic line. The asterisk marks a non-specific band close to PAR-6::mCherry (compare to N2 wt). **g**, Width of the point-spread function of membrane-associated fluorophores for GFP, as well as mCherry (**h**). Left side, fluorescence intensity profile of the 40 pixel band (8.7 μm) around the membrane (insert, original image). Right side, individual fluorescent intensity profile (black) and fit (blue), as explained above, with $\sigma_g = 344$ nm for GFP and $\sigma_g = 306$ nm for mCherry. Measurement of the ensemble-averaged cytoplasmic and membrane bound total amount of NMY-2, PAR-2 and PAR-6, for the following conditions **i**, *mlc-4* RNAi (N=8), **j**, *par-2* and *par-6* double RNAi (N=8 for NMY-2, N=10 for PAR-2 and PAR-6), **l**, PAR-2 MT- mutant (N=6 for NMY-2, N=9 for PAR-2 and PAR-6), **m**, unperturbed condition (N=8 for NMY-2, N=6 for PAR-2 and PAR-6). **k**, Individual point spread function of one 100 nm TetraSpeck fluorescent bead. Red and black: fluorescence intensity along the x and y direction. Blue: fluorescence intensity along the z direction. Open circles show the data, the solid line represents a gaussian fit to the data, yielding σ_x = 0.191 μm in x, σ_y = 0.173 μm in y and σ_z = 0.46 μm in z. **n**, The sum of the membrane-bound and cytoplasmic PAR-2 and PAR-6 amount in protein number, for the unperturbed condition (N=6) and *par-6* RNAi (N=6). **o**, The membrane-bound amount of PAR-2 and PAR-6 in protein number, for the unperturbed condition (N=6) and *par-6* RNAi (N=6). **p**, The sum of the membrane-bound and cytoplasmic PAR-2 and PAR-6 amount in protein number, for the unperturbed condition (N=6) and *par-2* and *par-6* double RNAi (N=10). **q**, The membrane-bound amount of PAR-2 and PAR-6 in protein number, for the unperturbed condition (N=6) and *par-2* and *par-6* RNAi (N=10). See section 'Determining total protein amounts, Methods' for details.

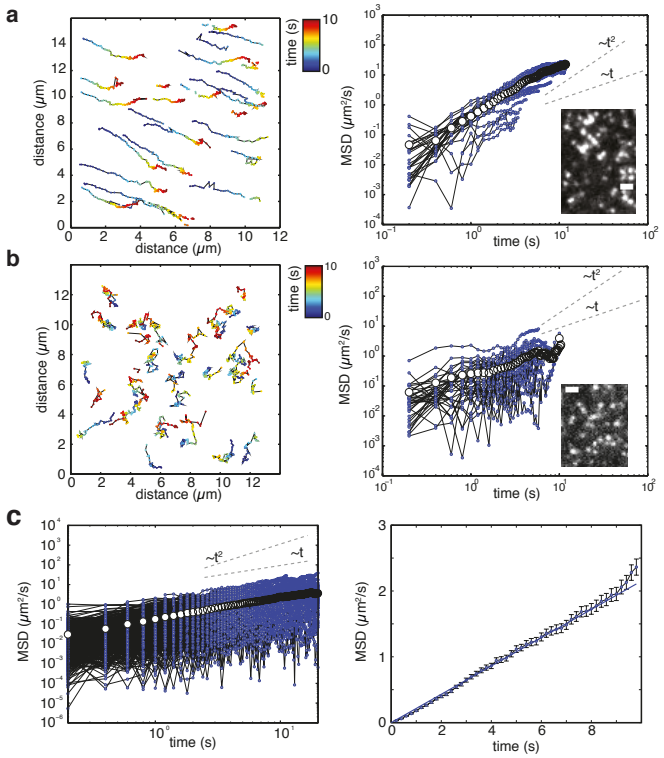

Fig. S4 – Measuring the NMY-2 diffusion constant. **a**, Trajectories and mean squared displacement of NMY-2 during the flow phase, for an individual movie. Blue dots: individual tracks, white dots: average. (Scale bar: 1 μm) **b**, Trajectories and mean squared displacement of NMY-2 during *ect-2* RNAi, for an individual movie. Blue dots: individual tracks, white dots: average. (Scale bar: 1 μm) **c**, Ensemble-averaged mean squared displacement of 7 movies, during *ect-2* RNAi. We restricted our analysis to tracks with a minimum length of 3 seconds (N=657 tracks). Blue dots: individual tracks, white dots: average. Fitting a mean squared displacement, linear in time resulted in D_M= 0.054 $\mu m^{2-1} \pm 0.081\ \mu m^2 s^{-1}$.

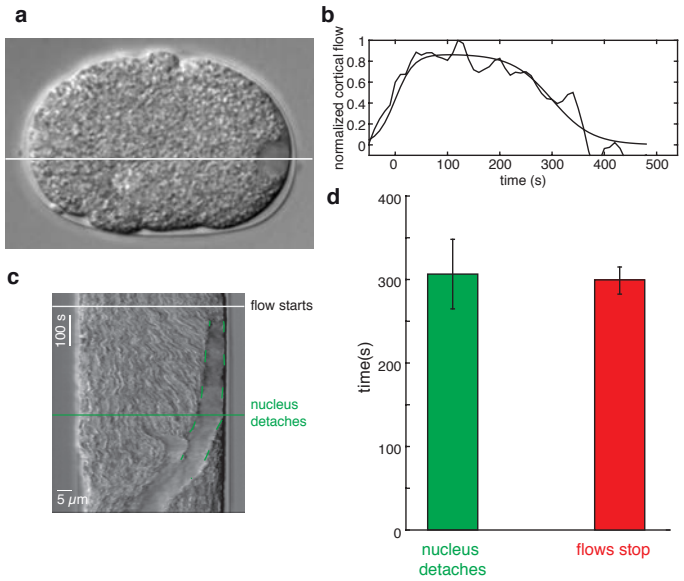

Fig. S5 – The actomyosin cue becomes inactive when the centrosome detaches from the cortex. **a**, DIC image of a one cell *C. elegans* embryo. The white line indicates the representative position of the kymograph, shown in **c**, Kymograph of DIC images, indicating two events: 1) Start of cytoplasmic flows, 2) Detachment of the male pronucleus from the cell membrane. This separates the centrosome, which is physically attached to the male pronucleus, from the actomyosin cortex. **b**, Temporal profile of the normalized average cortical flow profile in the posterior domain (between -30 µm to 30 µm, with respect to the posterior pole) on a data-set where DIC movies and NMY-2 fluorescence was measured in parallel (N=8). To extract the cessation of flows, we fitted this temporal profile with $f(t) = \frac{1}{2}\left[\tanh(\frac{t}{\tau_{\text{on}}}) - \tanh(\frac{t-T_{\text{stop}}}{\tau_{\text{off}}})\right]$, where T_{stop} gives the time when flows stop. **d**, Quantification of the average time between the start of flows and the moment where the nucleus detaches from the cell membrane as well as time between the start of flows and the cessation of cytoplasmic flows, extracted from the same data set (N=8). Error bars: 95% confidence interval.

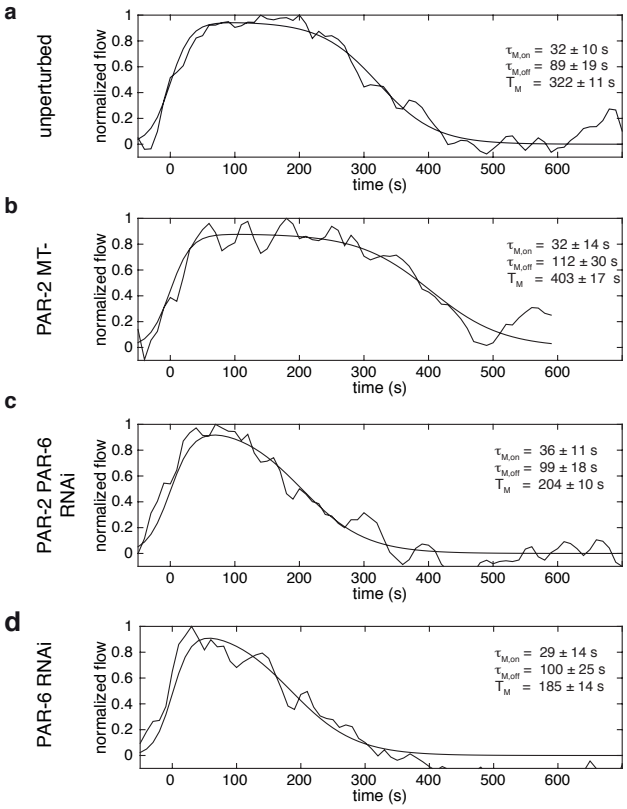

Fig. S6 – Temporal profile of normalized, averaged amplitude of cortical flows, induced by the the actomyosin cue. **a**, unperturbed condition (N=12), **b**, PAR-2 MT- (N=9), **c**, *par-2* and *par-6* double RNAi (N=10), **d**, *par-6* RNAi (N=11). For all conditions, the absolute value of the cortical flow field was averaged in space, over the posterior domain (between -30 µm to 30 µm, with respect to the posterior pole). We fitted the temporal profile with $f_M(t) = \frac{1}{2}\left[\tanh(\frac{t}{\tau_{M,\mathrm{on}}}) - \tanh(\frac{t-T_M}{\tau_{M,\mathrm{off}}})\right]$, where the results are summarized in Supplementary Table S3 . Errors represent the 95% confidence interval.

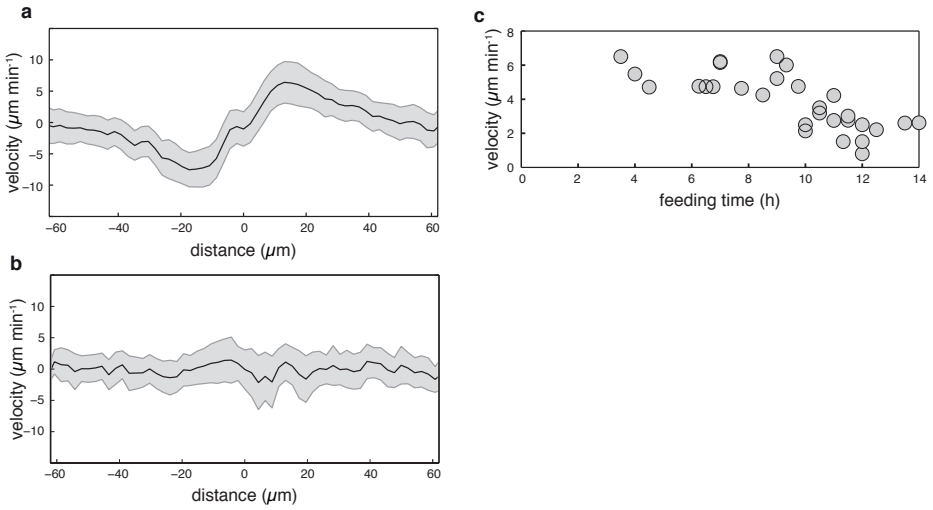

Fig. S7 – Actomyosin flows during *mlc-4* RNAi. **a**, Average of the cortical flow over 12 embryos and 100 s, for the unperturbed condition. **b**, Average of the cortical flow over 7 embryos and 100 s, for *mlc-4* RNAi. Error band represents the 95% confidence interval. **c**, Dependence of the cortical flow velocity on the *mlc-4* RNAi feeding time. We determined cortical flow velocities for *mlc-4* RNAi by investigating the displacement-field of yolk granules adjacent to the actomyosin cortex, using the freely available PIVlab MATLAB algorithm (*27*). 2D velocity fields were projected onto the anterior-posterior axis by dividing the embryo into 18 bins along the anterior-posterior axis, and by spatially averaging the x-component or the y-component of velocity along each bin in a single frame. The average velocity in each bin was then averaged over time across the entire flow period. The peak velocity was then determined as the maximum of the spatial flow profile.

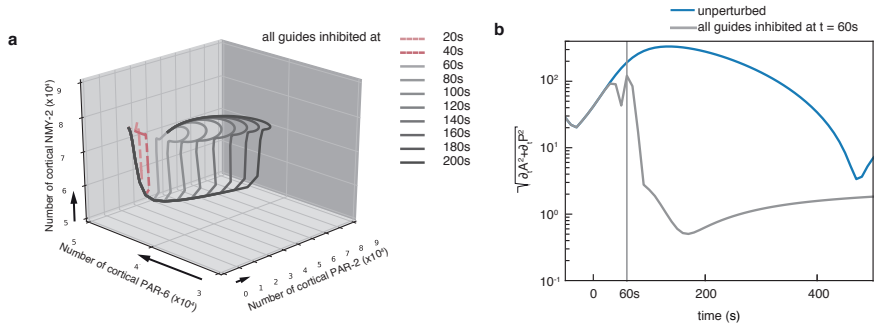

Fig. S8 – Characterizing the transition point. textbfa, Response of the PAR - actomyosin self-organization system upon cue inhibition at various time-points. Numerical simulation of the PAR - actomyosin self-organization system, shown analogous to Fig. 4a, main text, using unperturbed-condition parameters, when all three cues are disabled at time-points between 20s and 200 s. Note that for 20s and 40s, the system relaxes back to the initial state (homogeneous), while afterwards, it relaxes to the patterned polarity domain state. **b**, Speed of the PAR system, defined by $\sqrt{(\partial_t N_A)^2 + (\partial_t N_P)^2}$. Here N_A and N_P denote the number of cortical PAR-6 and PAR-2, respectively (see Fig. 4a, main text). The unperturbed condition (blue) is compared to the trajectory, for which all cues are disabled after the cues operate for 60s, just beyond the transition point.

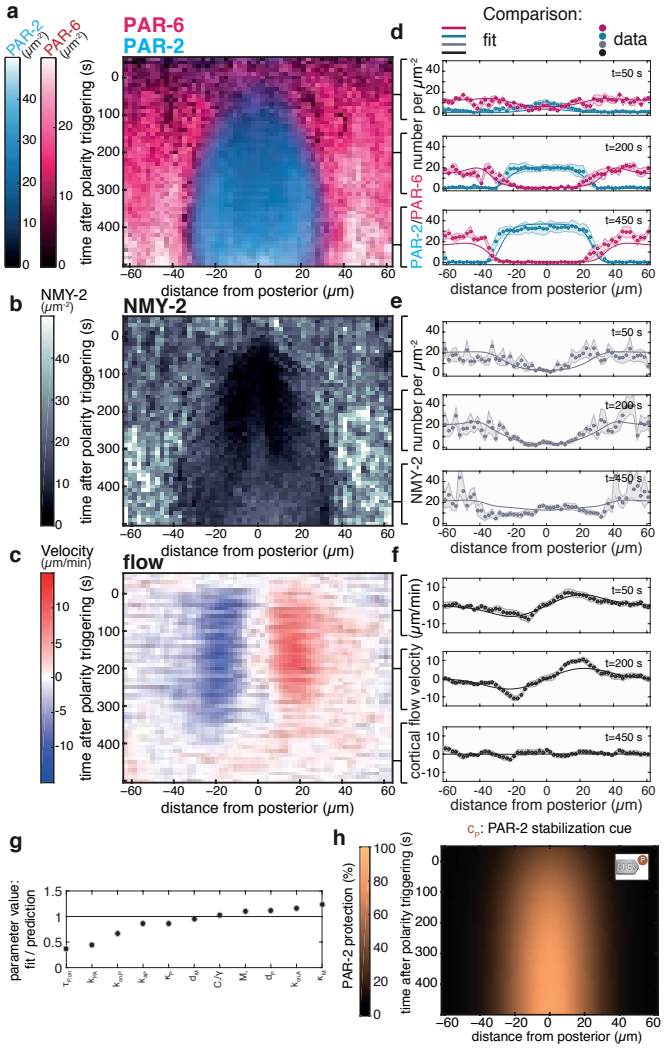

Fig. S9 – Fitting the unperturbed condition. a-c, Ensemble averaged concentrations of PAR-2::GFP, PAR-6::mCherry (N=6, both) and NMY-2::GFP (N=8) as well as the NMY-2 flow field (N=12) during polarity establishment, for the unperturbed condition. **d-f**, Comparison of the experimental PAR-2, PAR-6 and NMY-2 concentration profiles as well as flow fields (dots, shaded regions represent standard error of the mean) with the fit of the theory of guided mechanochemical self-organization, displayed at t=50s, 200s and 450s (solid lines), for the unperturbed condition (Supplementary Video 5). **g**, Ratio of the parameter values that have been fitted and the parameter values used for the prediction (Fig. 3k-m, main text). **h**, Spatiotemporal profile of the PAR-2 stabilization cue, obtained by fitting the unperturbed condition.

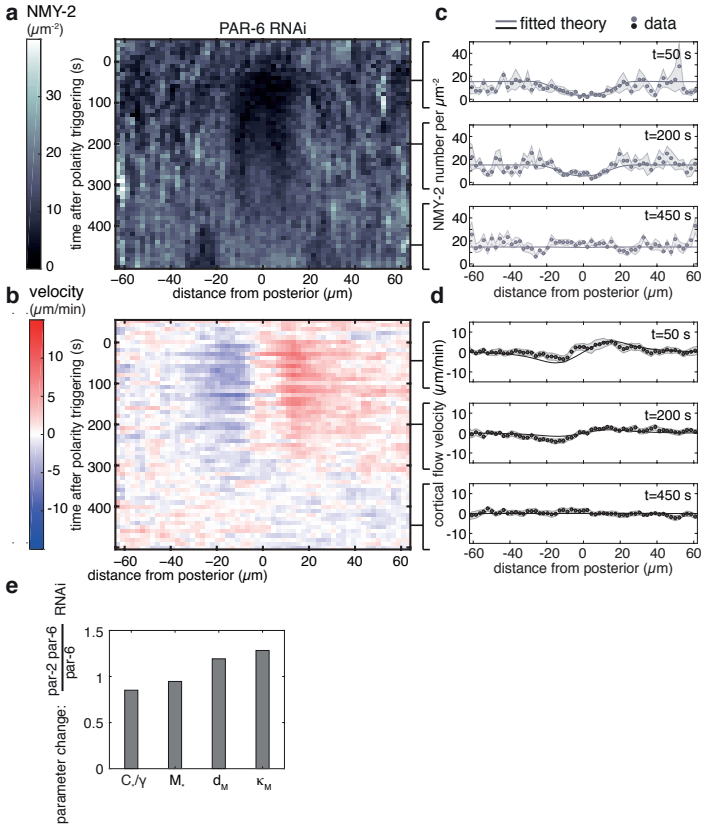

Fig. S10 – Quantifying the effect of the actomyosin cue on the NMY-2 system in isolation, during *par-6* RNAi . **a**, Kymograph of the ensemble averaged concentration field of NMY-2 (N=7) during *par-6* RNAi. **b**, Kymograph of the ensemble averaged flow field of NMY-2 (N=11) during *par-6* RNAi. **c**, Comparison of the experimental NMY-2 concentration profiles with the best fit, displayed at t=50s, 200s and 450s. **d**, Comparison of the experimental flow profile with the best fit, displayed at t=50s, 200s and 450s. **e**, Ratio of the parameters: C_*/γ (Contractility), M_* (Contractility saturation), d_M (width, myosin removal cue), κ_M (strength, myosin removal cue) from the *par-2* and *par-6* double RNAi condition over the *par-6* RNAi condition.

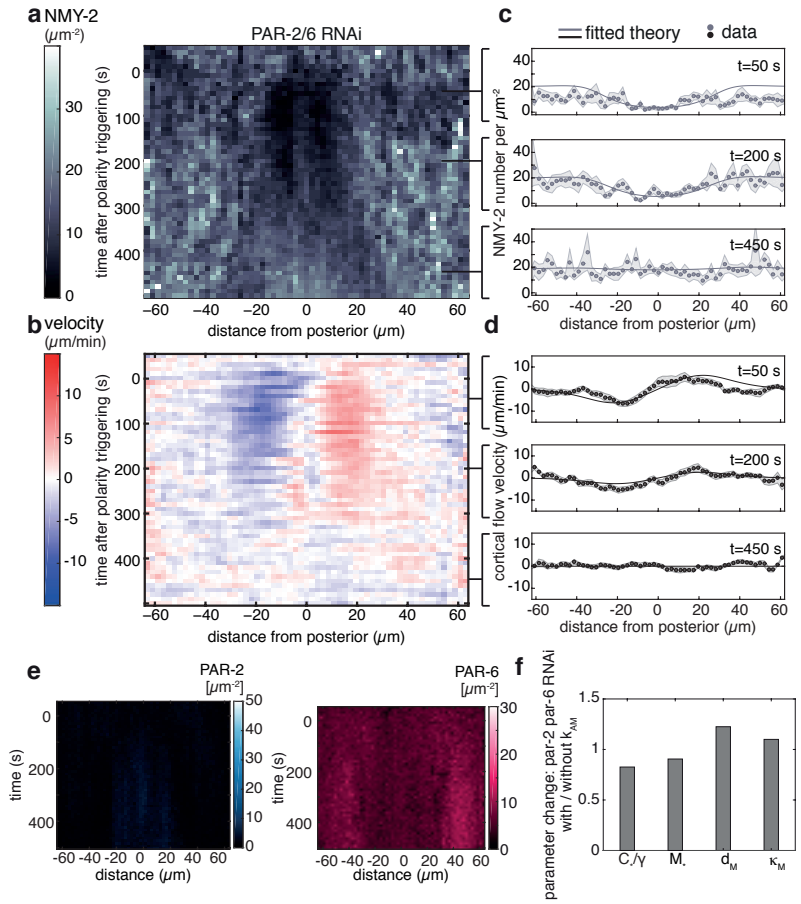

Fig. S11 – Fitting the NMY-2 - flow system, during *par-2* and *par-6* double RNAi, while also considering the experimentally measured PAR membrane concentrations. **a**, Kymograph of the ensemble averaged concentration field of NMY-2 (N=8) during *par-2* and *par-6* double RNAi. **b**, Kymograph of the ensemble averaged flow field of NMY-2 (N=10) during *par-2* and *par-6* double RNAi. **c,d**, Comparison of the experimental NMY-2 concentration profiles and flow fields with the best fit, displayed at t=50s, 200s and 450s. This fitting procedure explicitly considered the experimentally measured PAR-2 and PAR-6 concentrations (**e**). **f**, Ratio of the parameters: C_*/γ (Contractility), M_* (Contractility saturation), d_M (width, myosin removal cue), κ_M (strength, myosin removal cue) from the *par-2* and *par-6* double RNAi condition, obtained while ignoring the PAR concentrations over the best fit that explicitly considers the experimentally measured PAR-2 and PAR-6 concentration (**e**).

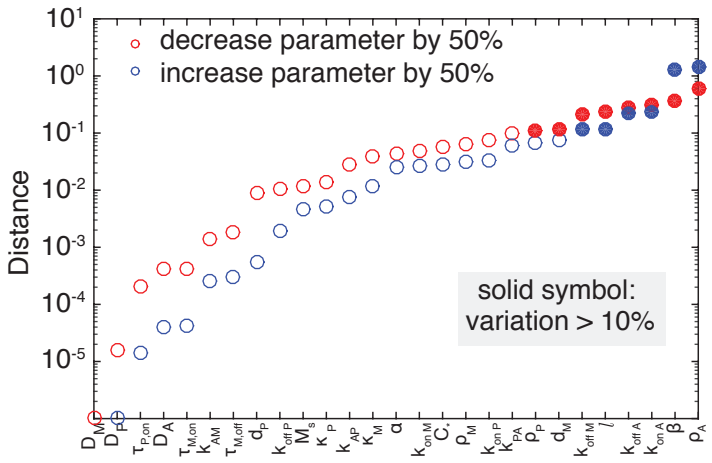

Fig. S12 – Parameter sensitivity analysis. Displayed is the distance measure (Supplementary Equation 50) between the unperturbed-condition solution and the model solution, where one parameter value is either increased or decreased by 50%. Solid symbols: variation of the solution is bigger than 10%.

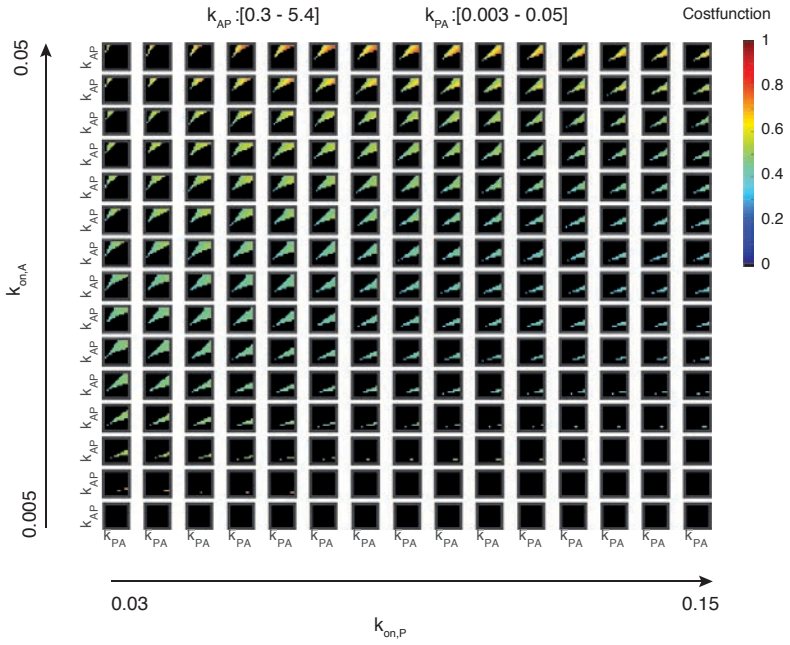

Fig. S13 – Cost-function when comparing the experimental *mlc-4* RNAi condition with the theoretical solutions. Four parameters were varied. Each box shows the cost-function against k_{AP} and k_{PA}, with a range between 0.3 - 5.4 μm^2 and 0.003 - 0.05 $\mu m^4 s^{-1}$, respectively. Boxes with increasing row number show the cost-function evaluated at increasing values of $k_{on,A}$, while increasing column numbers show values of increased $k_{on,P}$. $k_{on,A}$ was varied between 0.005 - 0.05 $\mu m s^{-1}$ and $k_{on,P}$ was varied between 0.03 - 0.15 $\mu m s^{-1}$. The cost-function is evaluated according to Supplementary Equation 48. Black regions indicate the parameter space where either the homogeneous A high state is unstable or the PAR reaction chemistry does not support multistability, or both.

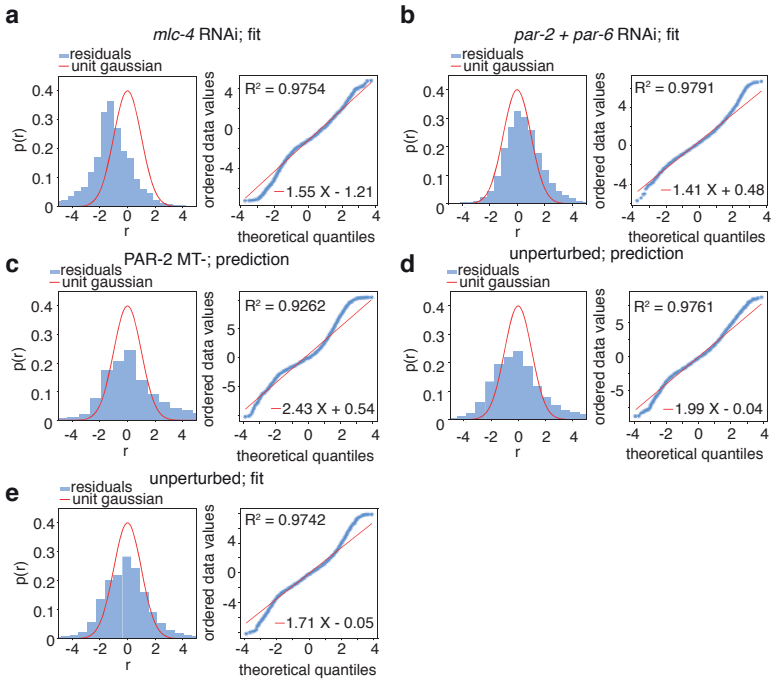

Fig. S14 – Quantifying the goodness of the fit / prediction for five conditions. **a**, *mlc-4* RNAi, **b**, *par-2* + *par-6* RNAi, **c**, PAR-2 MT- (*15*) prediction, **d**, unperturbed prediction, **e**, unperturbed, while fitting unknown parameters (Supplementary Fig. 9). We calculated the residuals between the experimental and theoretical results, which were normalized by the experimental standard error of the mean. For perfect agreement, this should yield a gaussian distribution with zero mean and unit width. To determine how well the experimental distribution agrees with the such a gaussian distribution, we also show quantile plots, which should, for perfect agreement, show a line with zero intercept and slope 1 (see Supplemental Information, section 2.6.1).

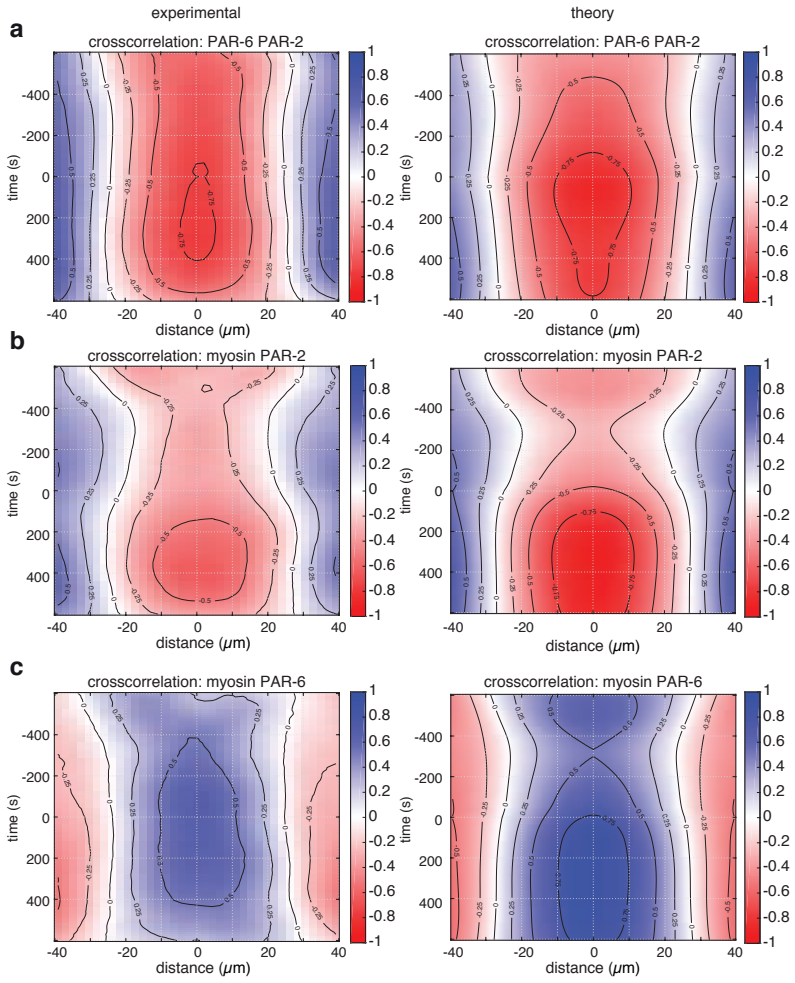

Fig. S15 – Normalized crosscorrelation between the PAR-2, PAR-6, and myosin concentration fields a, Comparison of the crosscorrelation between the ensemble-averaged experimental and theoretical concentration fields of PAR-2 and PAR-6 (N=6 for both). **b**, Comparison of the crosscorrelation between the ensemble-averaged experimental and theoretical concentration fields of myosin (N=8) and PAR-2 (N=6). **c**, Comparison of the crosscorrelation between the ensemble-averaged experimental and theoretical concentration fields of myosin (N=8) and PAR-6 (N=6) (see Supplemental Discussion).